Direct Numerical Simulation and Filtering of Turbulent Flows over Model Rough Surfaces

Nakayama, Akihiko
Sakio, Koji
Kitano, Yuya
Yokojima, Satoshi

Memoirs of the Graduate School of Engineering Kobe University
No. 1, pp. 9–41, 2009. doi:10.5047/gseku.e.2009.004

Direct Numerical Simulation and Filtering of Turbulent Flows over Model Rough Surfaces

Akihiko NAKAYAMA[1], Koji SAKIO[2] , Yuya KITANO[2] and Satoshi YOKOJIMA[3]

[1] *Department of Civil Engineering, Kobe University*
[2] *Software Cradle*
[3] *Department of Systems Engineering, Shizuoka University*

(Received November 20, 2009; Accepted February 26, 2010; Online published March 17, 2010)

Keyworkds: Turbulence, DNS, Rough Surface, Channel Flow, Large Eddies

Large-scale structures of flows over flat and wavy surfaces with and without two-dimensional and three-dimensional roughness waves on them, are studied numerically by first conducting Direct Numerical Simulation (DNS) of these flows at a Reynolds number in transitionally rough regime and numerically filtering the simulated results. A normalized kernel filter with a few different sizes and shapes that are applicable to flows near wall are used. The normalized positive filter smoothes the flow and the boundary by removing small-scale fluctuations and small-scale boundary protrusions at the same time. The characteristics of the extracted large-scale flows over the smoothed boundary and the effects of the removed sub-filter scale effects are studied in detail. Special emphasis is placed on the implications of the analyzed results in development and improvement of approximate simulation methods like Large Eddy Simulation (LES) of turbulent flows, where details of the flow and the boundary geometry cannot be resolved in full and modeling is needed. Filters with sizes that correspond to typical LES grid sizes remove considerable fraction of total fluctuations including correlated ones but the qualitative large structures are generally retained well if appropriate shape of the filter is used. The filtered large-scale flows over rough surfaces have similarities with the filtered flow over smooth surface with added resistance due to smoothed boundary. The effects of small boundary geometry removed by filtering are scaled by the filter size and the magnitude of the local velocity. Basic filtered equations of motion for near wall flows are also derived that can be used for rigorous analysis and modeling of interactions of the filter and the boundary.

1. Introduction

Large eddies and their structures have been known to control turbulent flows both qualitatively and quantitatively, but their exact behaviours depend strongly on the geometry and the overall boundary conditions that are different in individual flows and are difficult to generalize (e.g. Townsend [1)]). Smaller eddies, on the other hand, are mainly responsible for dissipating energy and are more isotropic with similarities. The Large Eddy Simulation (LES) method that tries to solve for the large-scale motion numerically can be an effective approach and has been intensively developed and extensively verified in recent years and are proving useful in various practical applications (e.g. Sagaut, [2)],Grinstein, Margolin & Rider [3)]). There are a few different basic approaches depending on how much of different scales of turbulent motion are resolved and how the effects of unresolved motion are represented (e.g. Pope [4)],Froelich & Rodi [5)]). The effects of unresolved scales are thought to be taken into account by modelling the subgrid scale (SGS) stresses that arise in the spatially-filtered governing equations of motion or by using appropriate numerical scheme that has an equivalent effect.

The large-scale flow, that is resolved by a numerical grid and computed directly, is distinguished from the original flow by some method of removing the small-scale fluctuations, by explicit filtering, by numerical solution method or by analytical representation. In either case, if the effects of unresolved small-scale motion are appropriately represented, the computed results are expected to be or to approach the original flow rather than to reproduce the filtered large-scale flow. Spatial filtering is usually used only as a theoretical basis to assume that spatial differentiation and filtering can commute and the resolved flow satisfies the same basic equations with added SGS stresses or their discretized equivalents. However, filtering of near wall flows not only violates the commutation assumption (Ghosal & Moin [6)]), but the definition itself is not straightforward (Galdi & Layton [7)], Sagaut [2)]). It may also be related to the difficulties of modeling wall effects in LES (e.g. Piomelli & Balaras [8)]). Solid boundaries determine the structure of the large-scale flows and it is very important to systematically investigate the wall-bounded flows in representing, interpreting and simulating turbulent flows of

realistic scales and situations.

In order to clarify the properties of large eddies of given scales in wall-bounded flows and their relation to the dynamics of near-wall flows, it is useful we study the details of the filtered flow field. Particularly, if flows filtered with given scales contain the basic turbulence processes such as the generation and maintenance of turbulence. It will also serve as a guide to evaluating and improving large eddy simulation methods of near wall flows over complex surface.

Since Direct Numerical Simulation (DNS) is now possible for various flows with small to medium Reynolds numbers, exact filtered flows can be examined with specific filtering applied to specific flows. However, the large-scale flows of simulated flows are rarely investigated from them. One reason is that filtering takes time almost as much as computing the flow itself and depending on the number of mean quantities to compute it requires large storage as well. In the present work, first we conduct DNS calculation of flows over model rough surfaces, and the results are spatially filtered to extract large-scale flow fields. This direct filtering unambiguously separates the large-scale flow and small-scale motion which we call 'sub-filter' scale motion. In doing this, a filtering method that is applicable to near-wall flows is defined and used so that the large-scale flows near rough walls can be studied. We will show that this procedure smoothes not only the flow but also the boundary itself so the smoothed boundary can be identified. Then we present basic equations that result from filtering the instantaneous Navier-Stokes equations over a finite and irregular flow domain. The added forces arise near solid boundaries need modelling if these equations are to be used for simulation of large-scale flows. In addition to the filtered flow fields, the conventional time mean and turbulence quantities are also documented so comparisons with other data of comparable configurations can also be made.

2. Direct numerical simulation of flows over model rough surfaces

In order to obtain the basic data for studying the filtered turbulent flows over rough and complex surfaces, first direct numerical simulations of flows over model rough surfaces on flat and curved surfaces are conducted. Since there are considerable amount of information both numerical and experimental, on flows over wavy walls, (Buckles, Hanratty & Adrian [9], Maass & Schumann [10], Hudson, Dykhno & Hanratty, [11], De Angelis, Lombardi & Banerjee [12], Cherukat et al. [13]; Henn & Skyes [14]; Calhoun & Street [15]) that can be made use of in verification and interpretation, we use a sinusoidal waviness as the basic geometry to construct more complex and general geometry. In many rough-surface flow investigations, angular roughness elements such as strip bars and blocks have been used as simplified models (e.g. Miyake, Tsujimoto & Nakaji [16]; Leonardi et al. [17]; Ashrafian, Anderson & Manhart [18]; Nagano, Hattori & Houra [19]; Choi & Suzuki [20]; Ikeda & Durbin [21]; Orlandi & Leodardi [22]). While they generate turbulence effectively with an unambiguous length scale, the boundary slope is discontinuous and not suited for filtering analysis. Discontinuous integrations are sometimes done when it comes to spatially averaging either experimental data or numerical simulation results of such flows (e.g. Ikeda & Durbin [21]). Sinusoidal waviness has discrete length scale that is better related to the scale of smoothing either by numerical or analytic approximations and wave-averaged velocity was computed from experimental data (e.g. Buckles et. al. [9]) and LES results (Henn & Sykes [14]). Also it resembles the roughness seen in industrial flows and natural environments.

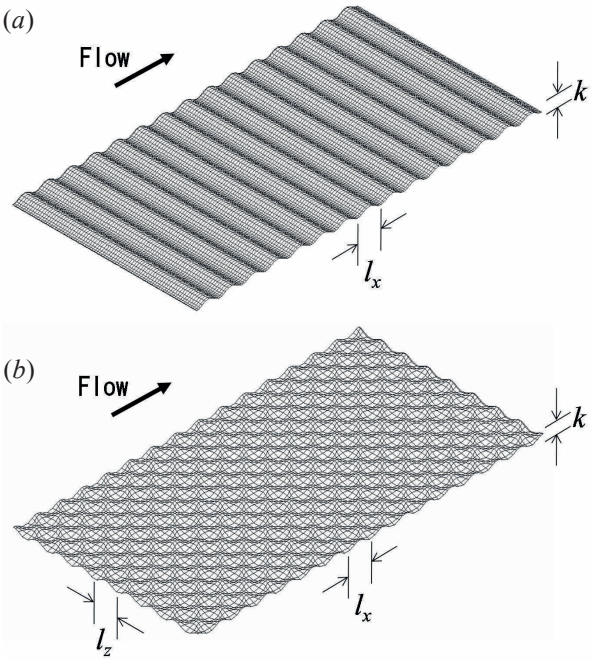

Fig. 1 Roughness models used for direct numerical simulation, (*a*) two-dimensional sinusoidal roughness R2, (*b*) three-dimensional sinusoidal roughness R3

2.1 Model roughness and simulated flow

Two types of analytical geometries have been chosen. The first one is a two-dimensional sinusoidal waviness that is uniform in the direction perpendicular to the main flow shown in Figure 1 (a). The vertical position of this surface $y_r(x)$ at streamwise position x is given by

$$y_r(x) = \frac{k}{2}\cos\frac{2\pi x}{l_x} \tag{1}$$

where k is the peak-to-peak height of the sinusoidal roughness and l_x is its wave length or the roughness pitch. This model is denoted in the following by R2. This sinusoidal waviness is similar in shape to many previous investigations of flows over wavy wall, but is noted that in the present simulation it is used to simulate roughness and the amplitude $k/2$ is only 2 percent of the channel height. The ratio of $k/2$ to the wave length l_x is 0.1 so that simulated flows at moderate Reynolds numbers separate on the down-slope side and reattach on the up-slope side (Buckles et al. [9]; De Angelis et al. [12]; Henn & Sykes [14]). The two dimensional roughness may be interpreted easier but there can be a fundamental difference between the two dimensional and three dimensional roughness. Therefore we also use a three-dimensional roughness generated by sinusoidal waves in two (x and z) directions tangent to the boundary shown in Figure 1(b). It is denoted by R3 and the equation for this is

$$y_r(x,z) = \frac{k}{2}\cos\frac{2\pi x}{l_x}\cos\frac{2\pi z}{l_z} \tag{2}$$

where l_z is the wave length in z-direction. This shape is the same as those used as a model of ripples in fluvial channel beds (Raudkivi [23]; Zedler & Street [24]). The geometric parameters of the two roughness geometries are summarized in Table 1. The solidity λ, defined to be the total projected frontal roughness area per unit wall-parallel projected area

Table 1. Details of shape and dimensions of roughness.

roughness name	Roughness type	height k	streamwise period l_x	spanwise period l_z	solidity λ
R2	2d roughness Figure1(a)	0.04	0.2	-	0.2
R3	3d roughness Figure1(b)	0.04	0.2	0.2	0.1

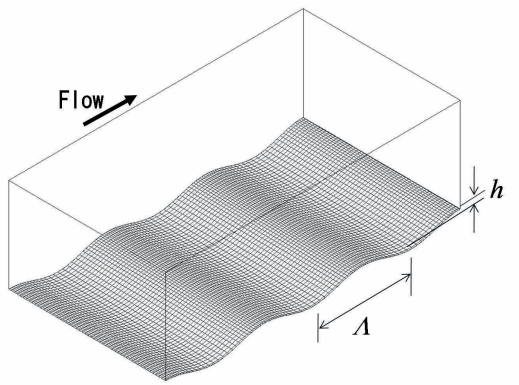

Fig. 2 Channel with wavy bottom surface.

Table 2. DNS run cases.

Case name	bottom surface	roughness	calculation region $LxHxB$	wave length Λ	wave amplitude h	Re_H HU_m/ν	average friction velocity U^*/U_m	viscous drag $D_f/\rho U_m^2$	pressure drag $D_p/\rho U_m^2$	applied pressure $\Delta pH/\rho L$
FS	flat	smooth	3x1x1.6	-	-	6760	0.0569	.003190	0	.00323
FR2	flat	R2	3x1x1.6	-	-	6763	0.0759	.001656	.003920	.00577
FR3	flat	R3	3x1x1.6	-	-	6751	0.0683	.003054	.001565	.00473
WS	wavy	smooth	3x1x1.6	1.0	0.05	6759	0.1009	.002339	.006765	.01022
WR2	wavy	R2	3x1x1.6	1.0	0.05	6764	0.1216	.000090	.012527	.01262
WR3	wavy	R3	3x1x1.6	1.0	0.05	6753	0.1098	.001157	.007681	.00884

U_m, cross sectional average velocity, $U^*=(\Delta pH/\rho L)^{1/2}$

(Schlichting [25]), is 0.2 for R2 and 0.1 for R3. These values of λ are near the border of the sparse and dense roughnesses and the equivalent sand roughness for R3 should be very close to the actual height of the waviness k, but for R2 we expect the drag coefficient to be larger and the equivalent sand roughness would be larger than k (Jimenez [26]) .

First, simulations of flows over these roughnesses placed on the flat bottom of a two dimensional channel are conducted. These flows are designated as FR2 and FR3. The mean and turbulence quantities are examined in the fully developed state keeping the Reynolds number based on the average cross sectional velocity U_m and the channel height H at nominally constant value of 6760. If the surface is smooth it corresponds to Re_τ (Reynolds number based on the friction velocity and the channel height) close to 395. The Reynolds number based on the peak to peak height k of the roughness is about 22 for R2 and 19 for R3, which are far smaller than that of fully rough flow but is in the transitionally rough range. Simulations at higher roughness Reynolds numbers are not impossible but we want the ratio of k to the channel height H be sufficiently small so that the direct effects of the roughness on the outer layer to be small.

Then similar simulations are conducted for the same roughnesses placed over gently varying wavy surface as shown in Figure 2. This wavy surface is another sinusoidal function given by

$$y_w(x) = h\cos\frac{2\pi x}{\Lambda} \tag{3}$$

where h is the amplitude and Λ is the wave length. The maximum slope is half that of the sinusoidal roughness of R2 and R3 but the flow separates downstream of the crests. In the following we call this a wavy surface and distinguish it from the smaller sinusoidal waves given by Eq.(1) or (2), which we call roughness for the purpose of clear designation. The wavy surface given by Eq.(3), particularly for the present value of h/Λ=0.05 has been used in previous experimental and wavy numerical investigations for studying turbulence characteristics by many workers (Maass & Schumann [10]; Hudson, Dykhno & Hanratty [11]; De Angelis et al. [12]; Charukat et al. [13]; Henn & Sykes [14]; Calhoun & Street [15]; Tseng & Ferziger [27]). This wavy surface creates acceleration, deceleration and even flow separations so the roughness effects on these rapidly changing flows can be studied. Flows with roughness R2 and R3 on this wavy surface are designated as WR2 and WR3, respectively. In order to validate the numerical method described below, and to obtain baseline flows, additional runs for flows over smooth flat channel without roughness designated FS and wavy smooth surface designated WS were conducted. Table 2 summarizes the conducted DNS runs. The numerical method used in the present work is the same as that described and verified in Nakayama & Yokojima [28]. It is similar to that developed by Zhang, Street & Koseff [29] and is based on a fractional-step method with semi-implicit time advancing of viscous terms and explicit advancement of convective terms. Collocated grid arrangement on general curvilinear coordinates fitting the curved boundaries is used. A few improvements are incorporated. The interpolation from the cell centered Cartesian velocity components to the contravariant velocity components on the cell surfaces uses more accurate method of Inagagi & Abe [30] and the convective terms are differenced by the second-order conservative scheme of Kajishima [31].

The computational region and the numerical grid used for WR3 calculation are shown in Figure 3. Every third grid line is shown for clarity. The ratios of length L, height H and width B of the computational region are shown in Table 2 and are taken about the same as the bottom half of DNS calculations of fully developed flows between parallel plates (e.g. Moser et al. [32]), since the present upper boundary is a slip surface and corresponds roughly to the centerplane between

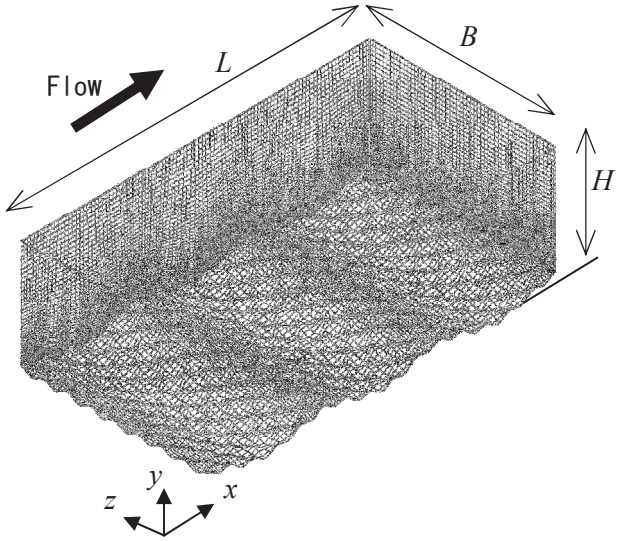

Fig. 3 Computational region and the numerical grid for WR3, every third grid line is shown.

parallel plates. There are 15 roughness waves in the calculation domain in the case of two-dimensional geometries of cases FR2 and WR2. In the cases of FR3 and WR3, there are 8 roughness waves in the spanwise z direction as well. The geometry and the flow are assumed to continue periodically in both streamwise and spanwise directions. In the wavy surface cases WR2 and WR3, three periods of waves are represented in the computational domain.

The number of grid points is 301x152x160 in the streamwise (x), wall-normal (y) and span-wise (z) directions, respectively, for all simulation cases. The grid spacing in y-direction is made smallest near the solid boundary at the bottom but largest at the top slip boundary. The the smallest grid spacing in terms of the average friction velocity U^*, reduced from the mean streamwise pressure gradient are (3.8, 0.25, 3.8) in the cases of smooth flow case FS. For FR2 and FR3 the shear stress at the top of roughness is about twice the average resistance so the viscous scale is about 40 percent smaller. The grid spacings in all directions are made smaller at the top of roughness and at the crest of waviness since the velocity gradient is larger there. For this purpose of optimizing grid density, gridlines are not exactly orthogonal but still very close to orthogonal (see Figure 3). One period of the wavy roughness is discretized by 20 grid points of the boundary fitting curvilinear coordinates. The same number of grid points is used for all cases and the grid spacings in terms of the local viscous scales vary around these values.

For each case the calculation was started from similar initial velocity field and advanced with time increment of $0.0005H/U_m$ over 100,000 steps for $50H/U_m$ then averages were taken over duration of $200\text{x}10^3$ steps over period of $100H/U_m$. U_m is the cross-sectional average velocity defined by the total volume flow rate divided by the average channel cross section $B\text{x}H$ and the Reynolds number based on H and U_m is set close to 6760 for all cases and close to that of the experiments of Hudson et al. [11], DNS of Maass & Schumann [10], LES of Henn & Sykes [14] and Calhoun & Street [15] and twice as large as Cherukat et. al. [29] DNS. The average pressure difference Δp between the upstream and downstream ends of the channel to maintain this Reynolds number and the corresponding friction velocity U^* are also shown in Table 2. The Reynolds number based on the average friction velocity U^* is 540 for FR2 and 450 for FR3 that are comparable to Moser et al. [32] DNS of closed smooth channel flow.

The results for the smooth wavy surface serve as a validation of the numerical procedure using the general coordinates by comparing with the existing experimental and numerical results. Figure 4 compares the presently calculated mean wall pressure $\langle p \rangle_w$ and mean wall shear stress $\langle \tau_{xy} \rangle_w$ for WS compared with the DNS results of Cherukat et. al. [13]. Angular brackets are used to represent time averages reserving the overbar to mean filter averages defined in the next section. The pressure distribution is very close to Cherukat et al.'s results but slightly pointed due probably to the difference in the Reynolds number. The shear stress also agrees very well but slightly lower, again due to higher Reynolds number in the present calculation.

Figure 5(a) compares the profiles of mean velocity $\langle u \rangle$ in x-direction and Figure 5(b) compares the Reynolds shear stress $-\langle u'v' \rangle$ distributions at ten streamwise locations within the basic period of the wavy surface. Single quotation is used to denote the deviation from the time average. Both mean velocity and the Reynolds shear stress are normalized by the mean friction velocity U^* implied by the applied pressure gradient. The present flow has a free-slip surface as the top boundary as opposed to the noslip boundary in the comparison cases of Hudson *et al*. [11] and Calhoun & Street [15], so even if half the channel height is used in place of the present full channel depth, there is some difference near the center of the channel where the velocity is smaller in the slip-wall channel of the present calculation. Other than these differences, both flows are very close and the consistency of the present simulation results with them indicates that the calculations are carried out correctly. The sinusoidal roughness used in the present study has similar shape as this wavy surface, and we expect they are represented similarly. As an independent check of consistency, Table 2 shows the viscous and the pressure drags obtained by integrating the surface viscous stresses and the pressure over the bottom surface compared with the average pressure gradient applied to the entire flow. The sum of the surface integrated drags is seen to agree with the applied pressure force within one percent. Also good agreement of the present time-averaged results of flow over flat smooth surface with existing DNS data shown in the following sections serves as additional validation. Preliminary results and validation with different grid spacings are reported also in Nakayama & Sakio [33].

2.2 The results of flows over flat rough surfaces

Although the ratio of the wave amplitude to wave length of the present configuration used as roughness is large ($k/2/l_x$=0.1), the amplitude relative to the channel height $k/2/H$ is only 0.02 and much smaller than previous investigations of wavy-wall flows and the magnitudes and the extent of disturbances due to the present roughness waves are quite different from them. Three-dimensional waviness of case FR3 has not quite been studied before. Therefore we first summarize the results of the flow over flat rough surfaces.

The mean velocity, the Reynolds shear stress, the turbulence intensity distributions and the mean wall stresses and the mean wall pressure distributions of cases FR2 and FR3 are shown in Figures 6 and 7, respectively. For case FR2, the averages are taken over time, over the width of the flow and at the same relative locations with respect to individual roughness waves. For case FR3 the averages are over time and at the same relative streamwise and spanwise positions with respect to the individual three dimensional roughness waves. Figure 6(a) through 6(e) show distributions in y-direction at the peak of the roughness, halfway from the top of the roughness to the bottom located straight downstream, at the bottom of the roughness and halfway from the bottom to the next peak. These profiles are obtained by interpolating the simulation results done in the curvilinear coordinates onto a rectangular grid. For the three-dimensional roughness case FR3, similar profiles at four

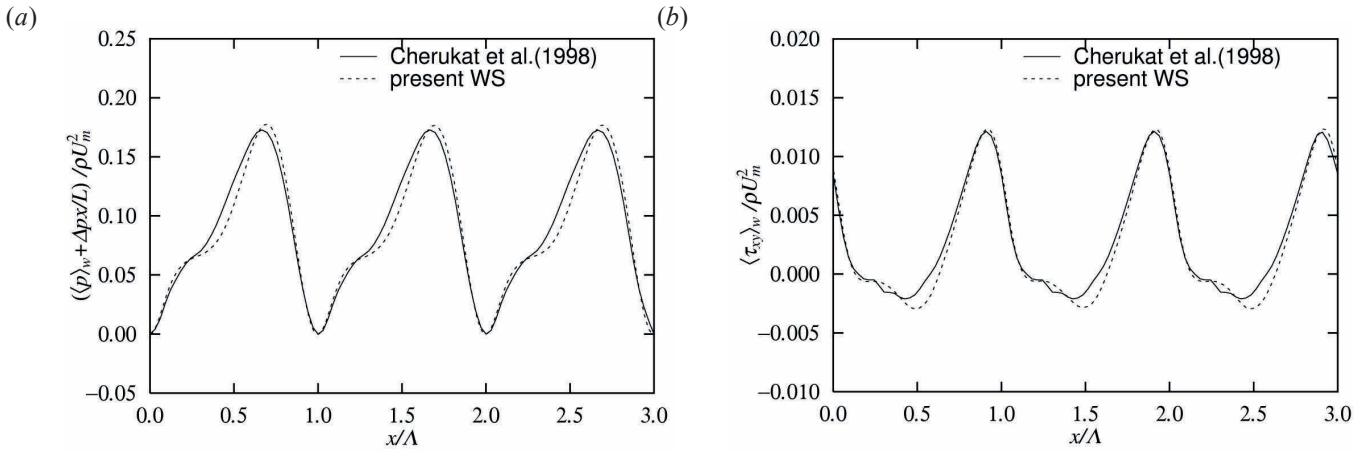

Fig. 4 Comparison of present calculation and previous DNS results. (*a*) wall pressure, (*b*) wall shear stress.

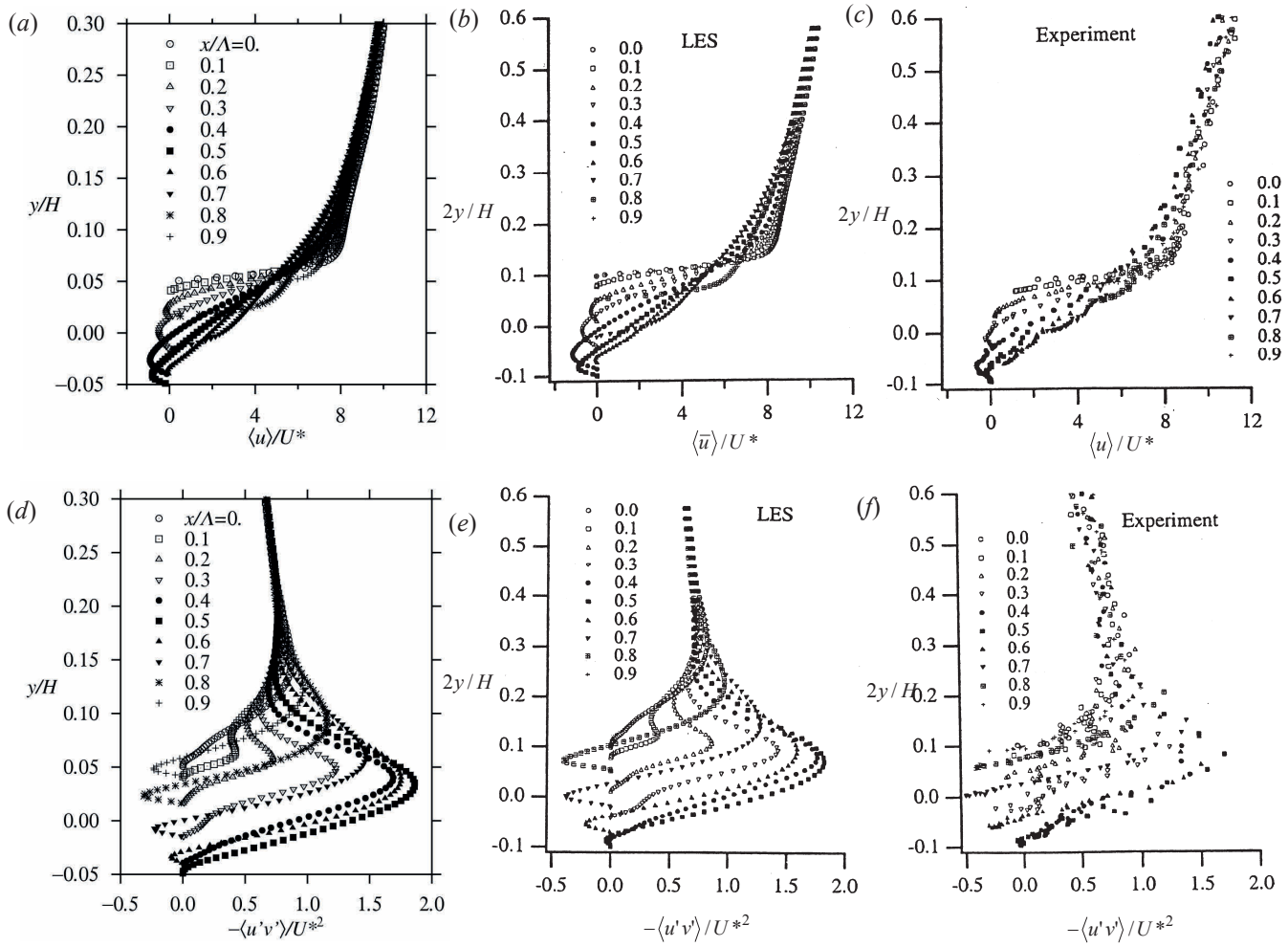

Fig. 5 Validation with flow over smooth wavy surface of mean velocity profiles. (*a*) present DNS, (*b*) Calhoun & Street (2001) LES, (*c*) Hudson et al.(1996), experiment, and Reynolds shear stress distribution, (*d*) present DNS, (*e*) Calhoun & Street (2001) LES, (*f*) Hudson et al.(1996), experiment.

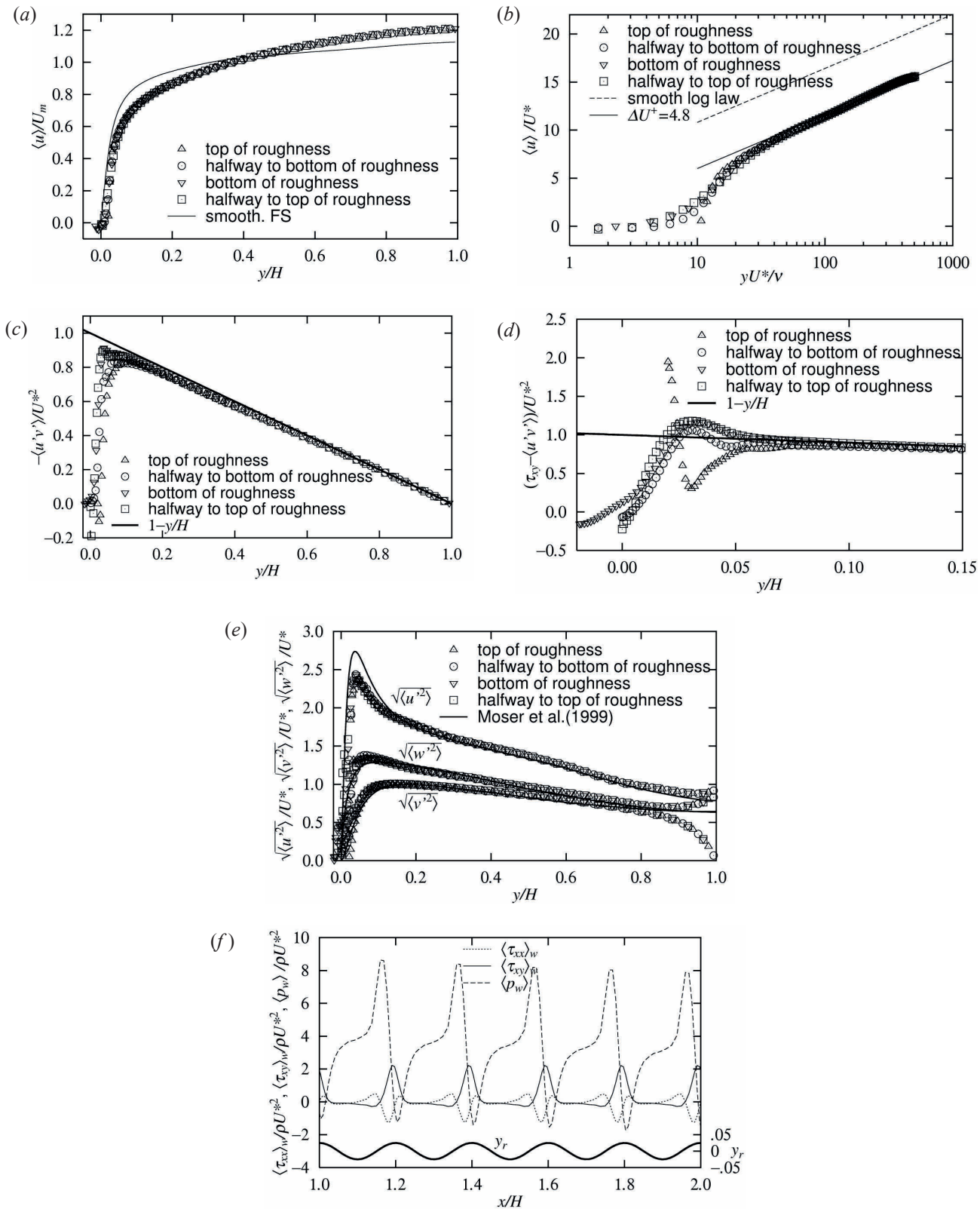

Fig. 6 Time-averaged results FR2 of flat surface with roughness R2. (*a*) mean velocity profiles in linear scale, (*b*) inner-law plot of mean velocity profiles, (*c*) Reynolds shear stress profiles, (*d*) total shear stress near wall, (*e*) turbulence intensities, (*f*) mean wall stresses and mean wall pressure. △, top of roughness; □, halfway to bottom of roughness; ▽, bottom of roughness; ○, halfway to top of roughness.

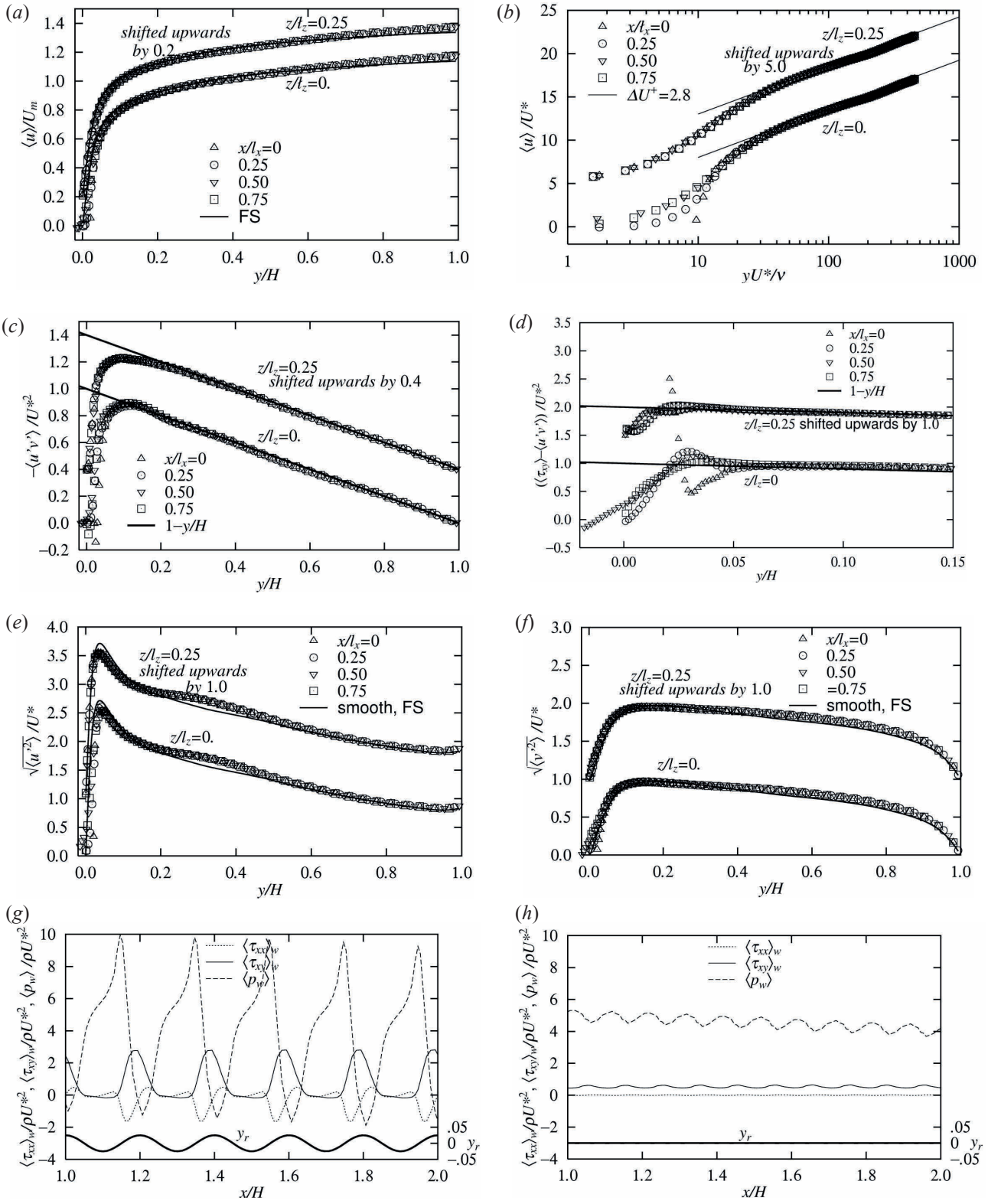

Fig. 7 Time-averaged results FR3 of flat surface with roughness R3. (*a*) mean velocity profiles in linear scale, (*b*) inner-law plots of mean velocity profiles, (*c*) Reynolds shear stress profiles, (*d*) total shear stress near wall, (*e*) streamwise turbulence intensity, (*f*) normal turbulence intensity, (*g*) mean wall stresses and mean wall pressure along z/l_z=0, (*h*) mean wall stresses and mean wall pressure along z/l_z=0.25, symbols same as Figure 6.

positions within one period of roughness along z/l_z=0 and at another set of four positions along z/l_z=1/4 are plotted in Figures7(a) through 7(f). The period or the wave length of the roughness is 0.2H in both x and z directions and z/l_z=0 is the streamwise plane along which the roughness peaks and troughs appear alternately. z/l_z =1/4 is the plane that cuts the bottom surface through midpoint between the peaks and troughs and the surface elevation is constant. Quantities are non-dimensionalized by the mean friction velocity U^* determined from the average streamwise pressure gradient. Every third y-position interpolated among actually calculated points is plotted for clarity except for the near-wall plots of Figures 6(d) and 7(d). The origin of y is taken, for the purpose of these plots, at the position of the mean boundary surface.

The mean velocity profiles are plotted in linear scale normalized by U_m in Figures 6(a) and 7(a) and compared with the smooth surface results. The inner-law plots based on U^* of the same data are given in Figure 6(b) and 7(b). Mean velocity at points below the average boundary position y=0 cannot be shown in these plots and the first point at the top of the roughness appears at about yU^*/ν=11 for R2 and 0.95 for R3. With this choice of presentation, points within yU^*/ν<10 are scattery, but points above yU^*/ν=30 are seen to fall on a single straight line that is very closely parallel to the usual smooth-wall log-law indicated by the broken line. The log-law with the shift of ΔU^+=4.8 is seen to fit the results of FR2 very well. The results of FR3 are seen to fit with ΔU^+=2.8 which is shown in Figure 7(b).

The Reynolds shear stress $-\langle u'v'\rangle$ distributions plotted in Figure 6(c) and 7(c) are seen to fall on the straight line 1-y/H above about y/H=0.16 for both cases, which corresponds to about 4k from the mean boundary. This is about the extent of the region known to be directly influenced by roughness (Raupach, Antonia & Rajagopalan [34]), and confirmed by experiments with angular roughness by Schultz & Flack [35]. The variations near the roughness are similar to the DNS results of Cherukat et al. [13] and at points near the top and on the upslope of the roughness the shear stress takes negative values but the magnitudes are smaller. The sum of the viscous stress $\langle\tau_{xy}\rangle/\rho=\nu\left(\partial\langle u\rangle/\partial y+\partial\langle v\rangle/\partial x\right)$ and the Reynolds stress $-\langle u'v'\rangle$ in the region y/H<0.15 is shown in Figures 6(d) and 7(d). The viscous stress contributions are large in the region y/H<0.05 and the values vary by large amount depending on the positions relative to the roughness. The total stress reaches 2U^* at the roughness peak while it is negative at the other three positions. Variations along z/l_z=0.05 of FR3 where the surface elevation happens to be constant, are seen to be much smaller than those along z/l_z =0.

The distributions of turbulence intensities in the streamwise direction $\sqrt{\langle u^2\rangle}$, wall-normal direction $\sqrt{\langle v^2\rangle}$, and spanwise direction $\sqrt{\langle w^2\rangle}$, all normalized by U^* are shown in Figure 6(e) for FR2 and $\sqrt{\langle u^2\rangle}$ and $\sqrt{\langle v^2\rangle}$ of FR3 in Figures 7(e) and 7(f). In Figure 6(e) of the case of FR2, the smooth-surface channel DNS results of Moser et al. [32] are shown for comparison, and those of FR3 are compared with the results of the smooth surface case FS. It should be noted again that in the present open-channel flow in which the boundary at y=H is a free-slip surface, the normal fluctuation is zero and the streamwise and the spanwise intensities are slightly larger than the closed channel case (Komori et al.,[36]; De Angelis et al. [12]; Nakayama & Yokojima [28]). Other than this difference, the turbulence intensity distributions away from the roughness influenced region, roughly y/H>0.15 are very close to the smooth channel result. Even in the near-wall region, the peak position of $\sqrt{\langle u'^2\rangle}$ is seen to be very close to the smooth flow case which is at y/H=0.08 and only twice the roughness height from the average position. Intensities are seen to be more isotropic with smaller streamwise intensity and larger normal intensity than the smooth-surface flow. Similar trends are also found in other rough surface flows (De Angelis et al. [12]; Ashrafian et al. [18]; Orlandi & Leonardi [22]).

The streamwise variations of the components $\langle\tau_{xx}\rangle_w$ and $\langle\tau_{xy}\rangle_w$ of the mean shear stress and the mean pressure $\langle p\rangle_w$ on the boundary, y=y_r are normalized by the applied total pressure force per unit length and width of the channel $\Delta pH/L=\rho U^{*2}$, are shown in Figure 6(f) and Figures 7(g) and 7(h). It is noted that the present pressure distributions are peakier than those over milder waviness of De Angelis et al. [12]. The shape of the rough boundary y_r in the corresponding plane is also shown for reference. The distribution of $\langle\tau_{xy}\rangle_w$ is consistent with the wall values of the total shear stress plotted in Figures 6(d) and 7(d). It is positive and large near the top of roughness and small and negative at the rest of the positions. The variations of the wall stresses and pressure are similar for two dimensional configuration of FR2 and along z/l_z=0 of FR3 where the boundary shape is identical. The variation of the wall pressure in either of these cases is much larger than that of the shear stress. It is also noted that the wall pressure and the wall stresses vary very little along z/l_z =0.25 along which the boundary shape happens to be flat. The average resistance is only about one half of the local maximum of $\langle\tau_{xy}\rangle_w$ but is much larger than its average. So neither the local value of $\langle\tau_{xy}\rangle_w$ nor its spatial average is appropriate to scale the mean flow. It is, of course, the property of rough surface flows. The exact values of the contributions of the viscous drag D_f and the pressure force D_p to the total resistance per unit surface area are listed in Table 2 for all simulated flows. It is seen that in the case of FR2 the viscous contribution is less than a half of the pressure-force contribution. These results underline once more that the local viscous stress or the friction velocity reduced from it is irrelevant to scale the local or global quantities and turbulent stresses. The large variation in the shear stress and the pressure near roughness are, of course, the main characteristics of rough surface flows which are more pronounced in higher Reynolds number flows, and are part of the motivation of examining spatially-averaged quantities in the next section.

The roughness function ΔU^+ obtained in the present simulation is plotted in Figure 8 against k^+ taken equal to kU^*/ν corresponding to the physical height of the roughness waves. As expected, the roughness function of the three-dimensional roughness is right on the uniform-sand roughness data in the transitionally rough regime taken from Schlichting [37]. ΔU^+ of R2 is seen to be a little larger than the Colebrook [38] fully rough-surface curve or recent data of honed surface measured by Schultz & Flack [35]. It is noted that Buckles et al. [9] found experimentally that the equivalent sand roughness height is about 2.4 times the peak-to-peak height of sinusoldally wavy roughness. The present result of FR2 also falls on the sand roughness if k^+ is taken a little more than twice the value based on the actual wave height.

Orlandi & Leonardi [22] proposed that the roughness function may better be correlated with the normal fluctuation intencity $\sqrt{\langle v^2\rangle}$ at the top of the roughness. In the present results, $\sqrt{\langle v^2\rangle}\Big/U^*\approx 0.4$ for both FR2 and FR3 at the top of roughness.

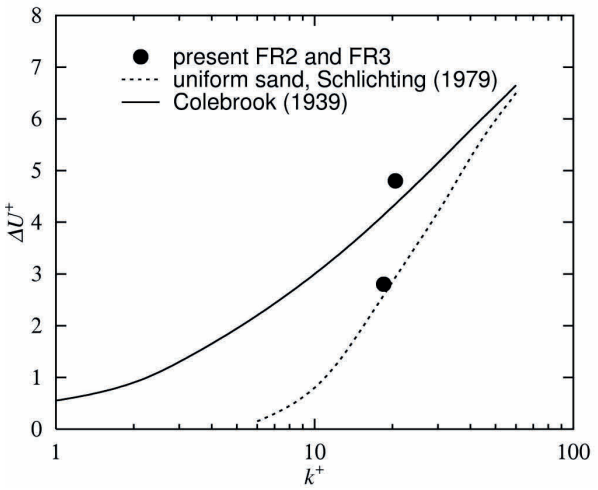

Fig. 8 Roughness function, ——, Colebrook (1939); ·····, uniform sand, from Schlichting (1979); ●, present FR2 and FR3.

Their correlation for this value of $\sqrt{\langle v^2 \rangle}/U^*$, implies ΔU^+=5.0 for both FR2 and FR3, contrary to the present result. Also $\sqrt{\langle v^2 \rangle}/U^*$ is seen to vary significantly near the top of roughness and is not easy to determine.

These simulation results of the flows over the present model sinusoidal roughness are what are generally expected from the known behavior of flows over flat rough surfaces in the transitionally rough regime and can serve as the baseline for studying their effects on more general flows over wavy surface.

2.3 The results of flows over wavy rough surfaces

Here we present the simulation results of flows over a wavy surface with the same roughness studied in the previous section. The purpose is, as explained earlier, to provide basic data of rough surface flows influenced by the changing pressure gradient with changing boundary and flow separation. Rough surface flows influenced by pressure gradient or acceleration and deceleration are studied experimentally by Gong, Taylor and Doernbrack [39] and Agelinchaab and Tachie [40] but not much is known. As seen in the validation case of WS shown in section 2.1, the pressure gradients caused by the waviness are large and the wall similarity based on the local friction velocity breaks down. In the case of WS the viscous drag contribution is about 32 percent of the total resistance. With roughness R2 on it, the viscous stress contribution diminishes to less than one percent of the total resistance and the pressure drag contribution takes over almost entire resistance (see Table 2). This is even smaller than the flow over angular roughness at a similar Reynolds number (e.g. Jimenez [26]). It is noted that in the case of the same roughness on flat surface FR2, the viscous drag contribution was as large as 30 percent, so the same roughness on a wavy surface has very different effects than on a flat surface. It should be recalled that the viscous stress is a local quantity determined by the velocity gradient on the boundary but the pressure drag is a result of uneven pressure distribution over an extended area of the boundary with varying surface slope and is a nonlocal effect depending on the flow structure of larger scales. The large waviness and the small roughness waves in the present study have similar shapes and the interpretation of the results as separate effects of roughness and the waviness may not be appropriate. It further motivates the present study to examine the flow similarity and the dynamic balance in terms of the spatially filtered flow field of the simulation results.

Figure 9 shows the distributions of mean wall pressure $\langle p \rangle_w$, and the viscous stress components $\langle \tau_{xx} \rangle_w$ and $\langle \tau_{xy} \rangle_w$ on the wall normalized by the dynamic pressure of the bulk flow ρU_m^2 for WR2 and WR3 compared with the wavy smooth surface results of WS along with the shape of the boundary $y_w + y_r$. It is seen that the pressure distribution over the wavy rough surface is composed of two components of variations. They are the variation with the period of the waviness $\Lambda=H$ that is similar to that of WS and the sharp peaks that correspond to the peaks of the roughness with period l_x=1/5H. So the streamwise pressure gradient is generally adverse from the top of the waviness to about 0.7H downstream and favorable from there to the top of the next peak. The wall shear stress, however, behaves differently. For the smooth case WS, the shear stress shows mild peak over the crest of the waviness, but for WR2 and WR3 the shear stress takes a spiky peak at the peak of roughness located on the crest of the waviness and the next peak corresponding to the next roughness is small. The shear stress stays low and may even be negative at the rest of the surface. So the viscous stress on the wavy rough surface comes mostly from the roughness peaks near the top of the waviness. It is interesting that the shear stress distribution along z/l_z=0.05 shown in Figure 9(*c*), where y_r=0 and the boundary shape happens to be the same as WS, is very close to that of WS shown in Figure 9(*a*).

Figure 10 shows the mean-velocity vectors together with the mean separation streamlines in the bottom half of the channel over one basic period of waviness of flows WS, WR2 and at two spanwise positions of flow WR3. They show separation behind every roughness wave and the separation streamline has wiggly shape opposite of the waviness of the boundary. The overall large-scale shapes of the separating streamlines, however, are similar. The roughness wave nearest the crest is seen to intensify the strength of the separated shear layer while the other roughness waves just make the separation streamline to undulate and do not contribute much to intensify the shear layers.

The profiles of the mean streamwise velocity normalized by the average cross-sectional mean velocity U_m is plotted in Figure 11 at six streamwise positions x/Λ =0, 1/6, 2/6, 3/6, 4/6 and 5/6 within one period of the waviness for cases WR2 and WR3 compared with the smooth wavy surface WS. The vertical coordinate is the onsdistance y-y_w from the wavy surface ignoring the roughness waves. There are five roughness waves in this basic period, and the first roughness peak of WR2 coincides with the top of the waviness. For WR3, the roughness peak and crest of waviness can coincide along z/l_z=0 but along z/l_z =0.5 the top of waviness is at the bottom of roughness. In the region approximately $(y-y_w)/H$>0.4 the velocity profiles are similar at all plotted stations. Although it is not shown here, the velocity distribution in this part of the flow can be collapsed on a log-law with the intercept corresponding to the that of rough-surface flow with roughness height colse to $2h+k$ (Nakayama & Sakio [33]). Very close to the surface the mean velocity of WR2 and WR3 vary widely. In the area between these two regions, 0.15<y/H<0.4, the effects of the roughness are not uniform. In the adverse pressure gradient region, x/Λ=1/6 to 4/6, the magnitude and the region of velocity reduction grow and in the accelerating region, x/Λ =5/6 to 1/6

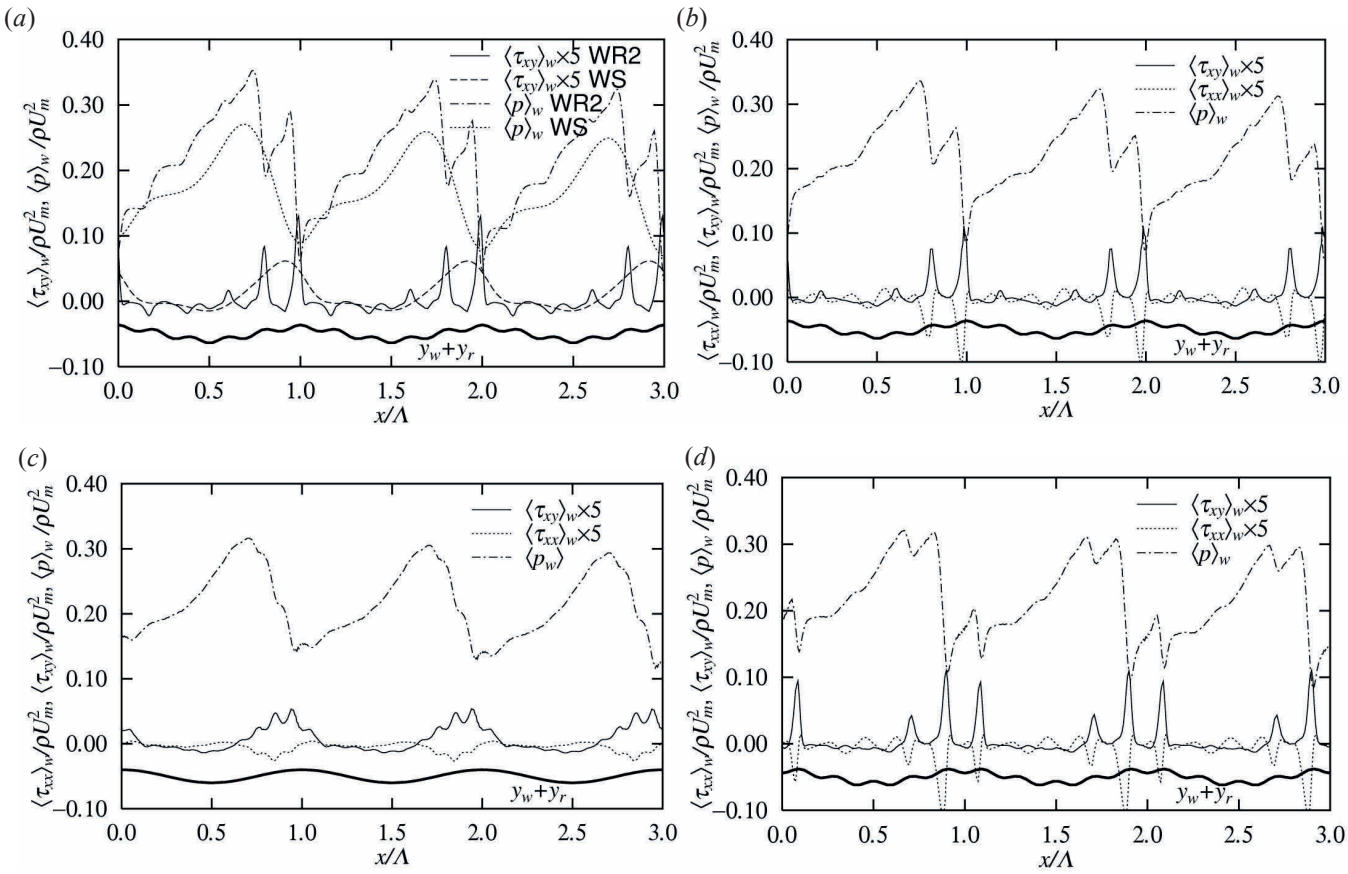

Fig. 9 Mean wall pressure and wall shear stresses. (*a*) WR2 compared with WS, (*b*) WR3, z/l_z=0, (*c*) WR3, z/l_z=0.25, (*d*) WR3, z/l_z=0.5. _ _ _ , $\langle p\rangle_w/\rho U_m^2$; ____ , $\langle\tau_{xy}\rangle_w/\rho U_m^2$; ..... , $\langle\tau_{xx}\rangle_w/\rho U_m^2$.

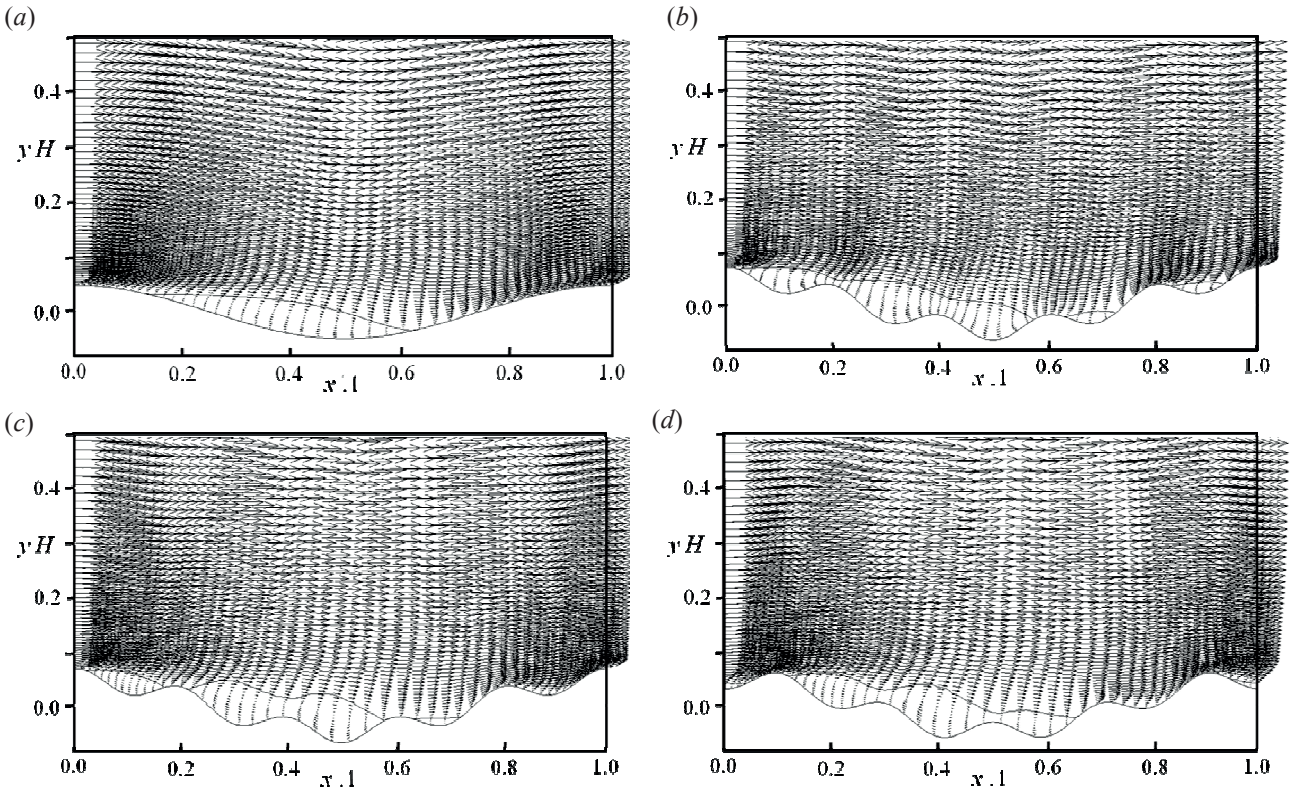

Fig. 10 Mean velocity vectors and the separation streamline. (*a*) WS, (*b*) WR2, (*c*) WR3, z/l_z=0, (*d*) WR3, z/l_z=0.5.

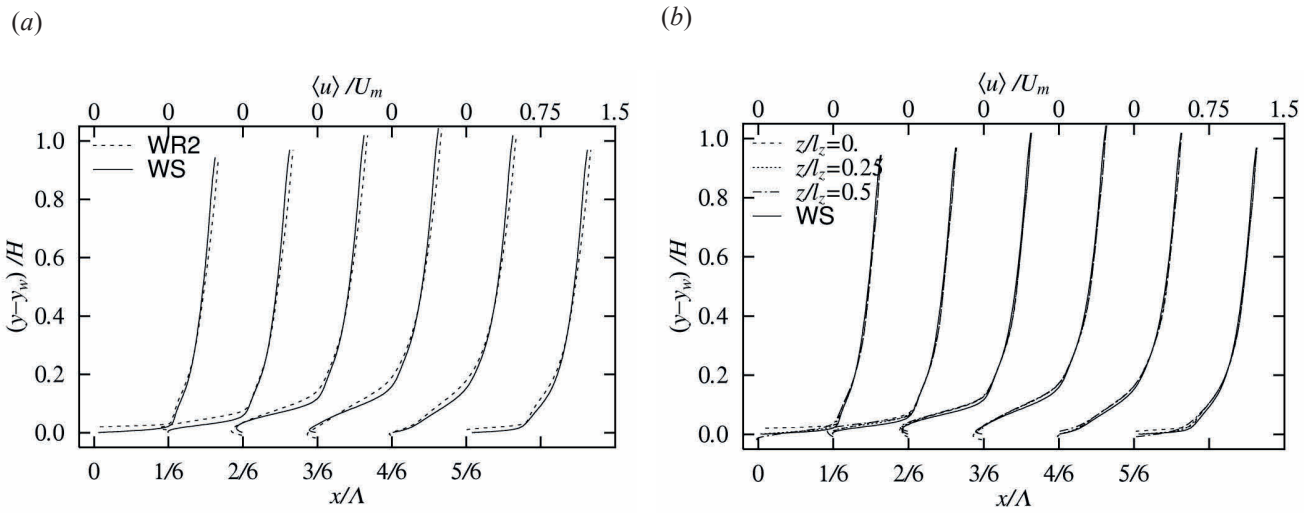

Fig. 11 Mean velocity profiles. (*a*) WR2compared with WS: ———, WS; - - - -, WR2, (*b*) WR3 compared with WS: ———, WS; - - - -, z/l_z=0; ·····, z/l_z=0.25; — · —, z/l_z=0.5.

they diminish. The parameter that this roughness effect can be correlated to, like the resistance in the flat wall case, must be a quantity that is not purely local but not totally global either. Purely local resistance is the wall shear stress that has sharp fluctuations of individual roughness. The global resistance is constant throughout the entire flow and is not appropriate either. It must be a quantity related to the flow with dimension possibly comparable to the thickness of the roughness-influenced region. This scale, that is not very obvious, may be quantified by the spatial filtering considered in the next section.

The Reynolds shear and normal stress components normalized by U_m^2 of cases WS, WR2 and WR3 are shown in Figures 12 through 15. Distributions only in the lower half of the basic period of the channel are shown. Contour lines are nearly horizontal in the region above about y/H=0.4 where time-averaged quantities are not directly influenced by the waviness or the roughness. The variations related to the waviness of period Λ are seen to be similar among these three cases and generally agree with the trends of previous simulations of similar wavy surface flows (De Angelis et al. 1997; Cherukat et al. [13]; Henn & Sykes [14]). That is, the shear stress and the streamwise normal stresses are large downstream of the crest of the large waviness just above the separated regions and smaller over the peaks of the waviness. The vertical and transverse components take local maximum slightly downstream mainly due to redistribution. It is also known that the shear stress $-\langle u'v' \rangle$ of the rectilinear components becomes negative in a wavy-wall flows of amplitude to period ratio similar to the present one. In Figure 12 the contour of zero shear is drawn in a thick line and it is seen that it is negative on the upslope surface of the waviness of WS. In the rough surface cases, it takes negative on the upslope surfaces of each roughness wave and very large negative on the upslope of the large waviness of WR2 case. The shape of the contours within one period is similar for all cases with wiggles and associated with the roughness waves and the overall increase of magnitude for cases WR2 and WR3. The strength of the large-scale separation downstream of the crest of the waviness appears the determining factor. The transverse component $\langle w^2 \rangle$ takes large values in upslope region near x/Λ=0.75 in all cases as seen in the smooth flows of WS and those of Cherukat et al. [13] and Henn & Sykes [14], but in the rough surface cases of WR2 and WR3 small increases are seen on the upslope surface of individual roughness waves. The maximum values of all these Reynolds stresses of the rough surface cases are larger than the smooth case WS and are largest in the case of WR2 and appear to be roughly proportional to the overall resistance shown in Table 2. As to the way the roughness waves contribute to the added resistance and the turbulence, they do not seem to necessarily create extra stresses locally downstream of the individual roughness waves. They just intensify the turbulence created by the crest of the large waviness. Also the roughness waves in the low-velocity region of the large-scale flow do not create as much turbulence as that in un-separated high velocity region. This implies that the effects of the small roughness are not quite local but not as large as the period of large waviness either. Similar results are implied by the experiments of Agelinchaab & Tachie [40] of rough surface flow in pressure gradient.

As seen from the wall stress plots of Figure 9, the wall stress has significant values only at a few roughness peaks near the top of the waviness and very small values at the rest of the locations, and therefore the local stress is not a good scale for the mean velocity. The simulation results of wavy rough surface flows compared with the results of flat rough surface flows indicate that the effects of the large streamwise pressure gradient caused by the large undulation of the boundary dwarf the disturbances caused by the small boundary irregularities presently interpreted as roughness. It is noted that in rough-surface flows the largest roughness dominates the effects that has also been found by by Miyake et al. [16] and Ikeda & Durbin [21]. It indicates as expected at the beginning that the small geometric irregularity of the boundary is overwhelmed by the large undulation and the effects of small boundary irregularity may have similarities that may be modeled. The filtering of the flow and the boundary as done in the following section will have important clues as to these questions.

3. Spatial filtering of flow and flow domain

In order to study what the large-scale flows that can be obtained by spatial filtering really are, and how they are related to the large structures that characterize the dynamics of specific turbulent flows, we apply filtering to the results of the DNS simulations described in the previous section. The objectives here are to study the detailed properties of the spatially filtered flow field, and to obtain the large-scale structures of the original flow and then to examine relevance to the modelling of small-scale flow and the effects of roughness and other boundary irregularities and also to gain insight into numerical

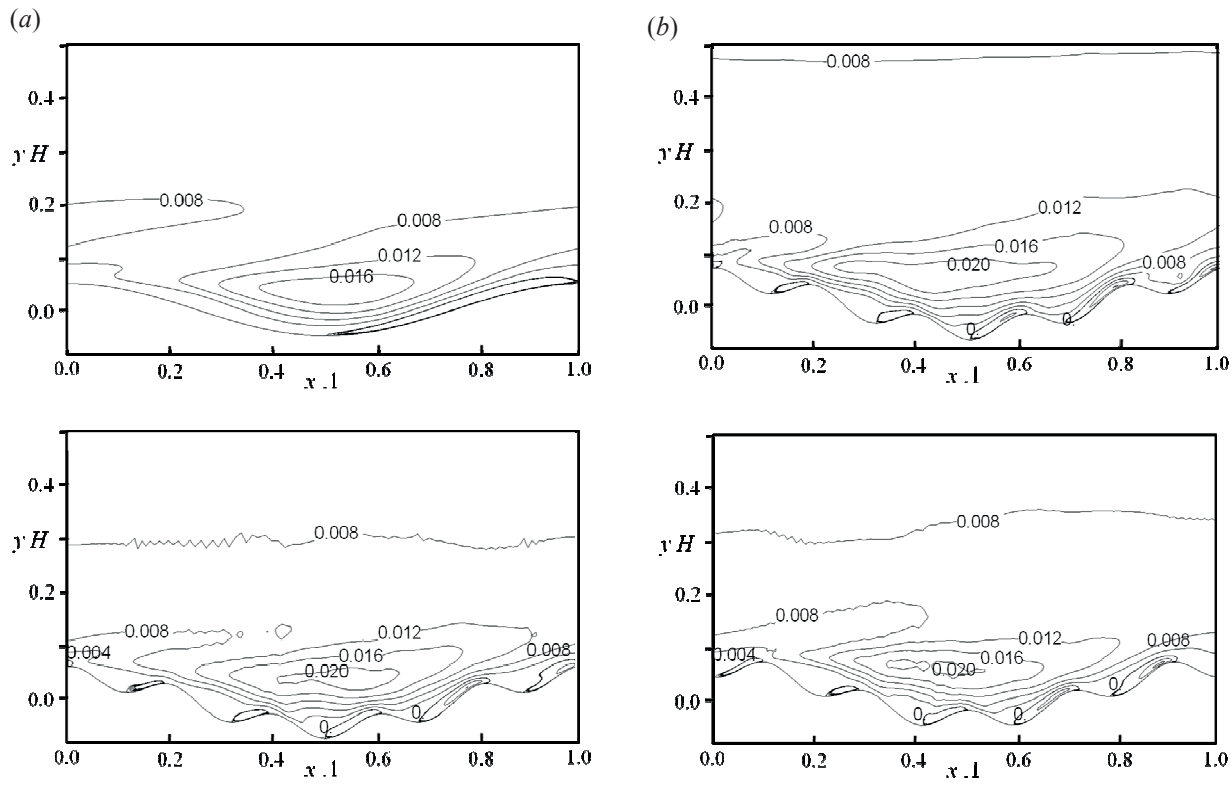

Fig. 12 Reynolds shear stress $-\langle u'v' \rangle$ normalized by U_m^2. (*a*) WS, (*b*) WR2, (*c*) WR3, z/l_z=0, (*d*) WR3, z/l_z=0.5.

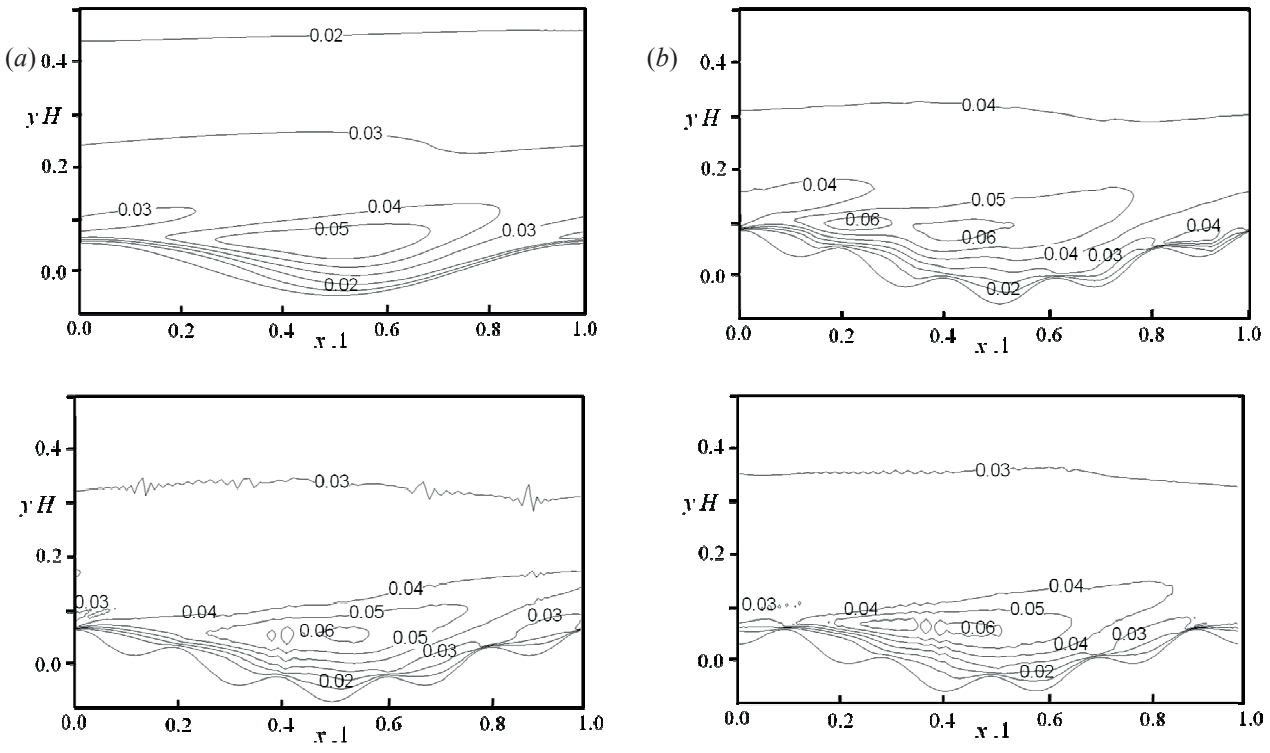

Fig. 13 Reynolds normal stress $\langle u'^2 \rangle$ normalized by U_m^2. (*a*) WS, (*b*) WR2, (*c*) WR3, z/l_z=0, (*d*) WR3, z/l_z=0.5.

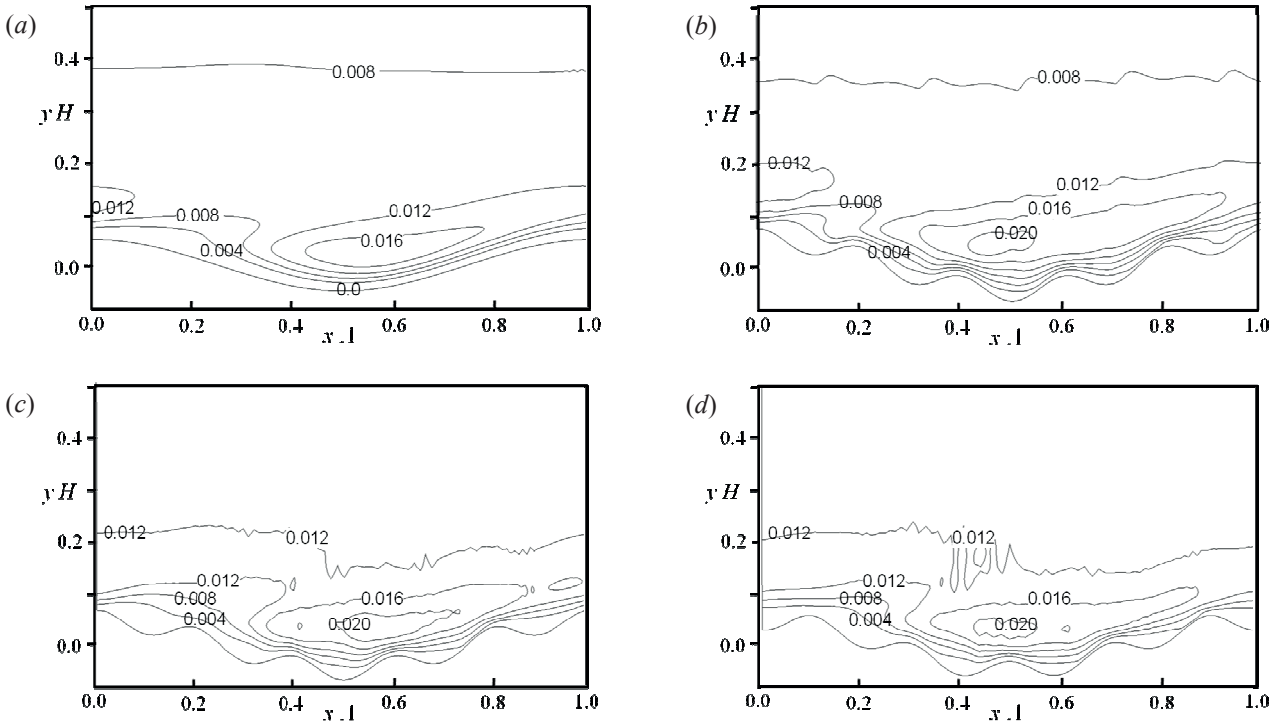

Fig. 14 Reynolds normal stress $\left\langle v'^2 \right\rangle$ normalized by U_m^2. (*a*) WS, (*b*) WR2, (*c*) WR3, z/l_z=0.0, (*d*) WR3, z/l_z=0.5.

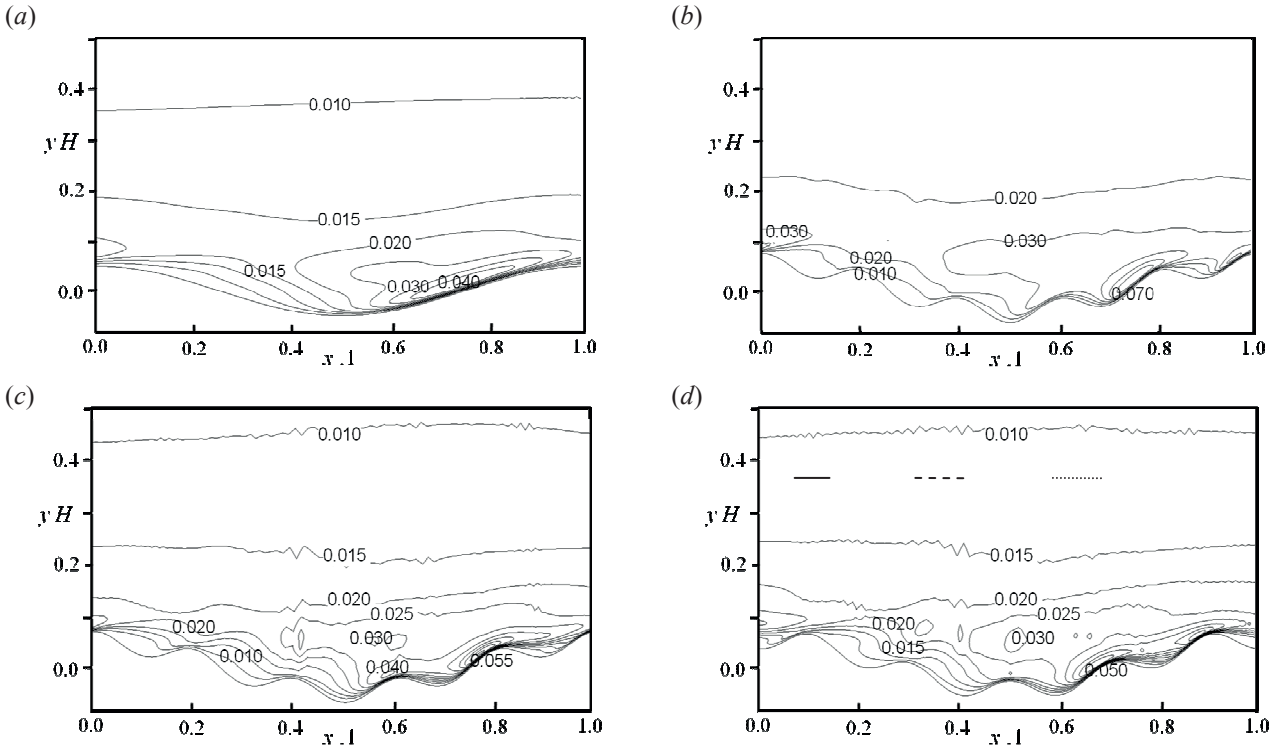

Fig. 15 Reynolds normal stress $\left\langle w'^2 \right\rangle$ normalized by U_m^2. (*a*) WS, (*b*) WR2, (*c*) WR3, z/l_z=0.0, (*d*) WR3, z/l_z=0.5.

modelling methods of large eddies. The results will also give quantitative data with which quality and accuracies of large eddy simulations can be evaluated. In most LES, spatial filtering defined by a convolution integral in infinite space is assumed (e.g. Pope [4]; Sagaut [2]), but it is used only to derive basic mathematical properties of filtering in infinite region. We like to apply a kernel filtering directly to the simulated flows that are in finite domain with complex boundary geometry. To do it, it is necessary to use a filtering procedure that is applicable to flows with boundary, including complex and rough surfaces. Filtering flows near boundary is not trivial (e.g. Galdi & Layton [7]; Sagaut [2]). We use a kernel filter that is normalized but not necessarily conservative (Vreman [41]). If the filter is not conservative, the filtered governing equations do not conserve mass or momentum without commutation terms (Ghosal & Moin [6]). We treat these non-commutative terms carefully and examine their properties. Also with this filtering method, the flow domain can be filtered at the same time and with the same filter applied to the flow. We use the top-hat filter for the sake of simple algorithm and examine, by changing the size and the ratios of the filter widths in three directions, what filtering often assumed implicitly or explicitly in LES calculations actually does to the flow and to the boundary. The characteristics of the top hat filter are given in Pope[4]. We also examine what differences there are between the three-dimensional the box filter and a plane filter often presumed in flows near boundary, and also the spanwise one-directional filter frequently used when explicit filtering is carried out as in dynamic procedures of determining model coefficients. The details will be explained in the following section.

3.1 Kernel filter

Let $f(\boldsymbol{x})$ be a flow quantity defined at point $\boldsymbol{x}$ in flow domain D, and we define its filter $\overline{f(\boldsymbol{x})}$ by a kernel integral

$$\overline{f(\boldsymbol{x})} = \iiint_D G(\boldsymbol{x},\boldsymbol{\xi}) f(\boldsymbol{\xi}) d\boldsymbol{\xi}\,, \tag{4}$$

where G is the filter kernel function that satisfies conditions

$$\iiint_D G(\boldsymbol{x},\boldsymbol{\xi})\, d\boldsymbol{\xi} = 1$$

and

$$G(\boldsymbol{x},\boldsymbol{\xi}) \geq 0 \quad \text{for all } \boldsymbol{\xi} \text{ in } D. \tag{5}$$

The first condition means that the filter is normalized, the second condition means it is positive and together they insure smoothing of function $f(\boldsymbol{x})$, in the sense that the filtering reduces the total variation (Vreman [41]). This is not the only choice of filter. Galdi & Layton [7] and Battacharya et al. [42] assume that there is flow with zero velocity outside the actual boundary and take a spatial integral over a filter scale larger than the distance to the boundary. This filtering does not assure smoothing of the resulting velocity distribution (Vreman [41]) and is not quite suited for LES where the purpose of filtering is to smooth the distribution that can be represented by a numerical grid used in the calculation. When the flow domain D is infinite or when the support of G is away from the boundary of D, Gaussian or top-hat weight functions with argument $\boldsymbol{x}$ - $\boldsymbol{\xi}$ for G satisfies these conditions. $G(\boldsymbol{x},\boldsymbol{\xi})$ is then symmetric with respect to $\boldsymbol{x}$ and $\boldsymbol{\xi}$ and the filtering operation defined by Eq.(4) commutes with spatial differentiation. When the support of D interferes with the boundary, G that satisfies the normalization condition depends on the flow geometry and the filter becomes non-uniform. G that is normalized and positive can be constructed from a conventional weight function $w(\boldsymbol{x})$ such as Gaussian or top-hat function satisfying condition Eq.(5) for the infinite domain, by

$$G(\boldsymbol{x},\boldsymbol{\xi},\boldsymbol{\Delta}) = \frac{w(\boldsymbol{\xi}-x,\boldsymbol{\Delta})}{W(\boldsymbol{x})}\,,$$

where

$$W(\boldsymbol{x}) = \iiint_D w(\boldsymbol{\xi}-x,\boldsymbol{\Delta}) d\boldsymbol{\xi}\,, \tag{6}$$

and $\boldsymbol{\Delta}$ is a vector indicating the filter widths in three directions. With this definition of G, $\overline{f(\boldsymbol{x})}$ is defined at any point where $W(\boldsymbol{x}) > 0$. For a flat or simple boundary, $\boldsymbol{\Delta}$ may be made to depend on the distance to the boundary to safisfy the normalization condition. In this case $G(\boldsymbol{x},\boldsymbol{\xi})$ is not symmetric either and the filter scale must diminish to zero as the boundary is approached. An alternative definition of normalized filter is

$$\bar{f}(\bar{\boldsymbol{x}}) = \iiint_D G(\boldsymbol{x},\boldsymbol{\xi},\boldsymbol{\Delta}) f(\boldsymbol{\xi}) d\boldsymbol{\xi}\,,$$

where

$$\bar{\boldsymbol{x}} = \iiint_D G(\boldsymbol{\xi}-x,\boldsymbol{\Delta})\boldsymbol{\xi}\, d\boldsymbol{\xi}\,. \tag{7}$$

This definition appears more plausible for complex boundaries including those with non-connected flow domains but the filtered function is an implicit function of a position and is not quite convenient to apply to terms in the equations of motion as we do in the following section. Since one of the objectives of the present work is to examine the flow filtered with large filter widths even at positions near the boundary so that requirements of LES not resolving the near-wall flow can be examined, we choose to take the first approach of using the normalized conventional weight function. In this case, if ∇_x and ∇_ξ are the differentiation operators with respect to $\boldsymbol{x}$, and $\boldsymbol{\xi}$, respectively,

$$\nabla_x G(\boldsymbol{x},\boldsymbol{\xi}) = -\nabla_\xi G(\boldsymbol{x},\boldsymbol{\xi}) - \frac{\nabla W}{W} G(\boldsymbol{x},\boldsymbol{\xi})\,, \tag{8}$$

and the differentiation of G with respect to $\boldsymbol{x}$ and the negative of differentiation with respect to $\boldsymbol{\xi}$ differ by the quantity related to the gradient of W. This term is related to the direction normal to the filtered boundary. $W(\boldsymbol{x})$ is a measure of the volume of the averaging region contained in the flow. It takes its maximum value W_m when point $\boldsymbol{x}$ is well inside the flow region, but it decreases as the boundary is approached. It will be zero if $\boldsymbol{x}$ is far outside the flow domain. Therefore $W(\boldsymbol{x})$ may be used to define the filtered boundary. For example $W(\boldsymbol{x})=1/2\,W_m$ is the border line where half of the un-normalized weight w comes from inside the flow and the other half from outside and can be used as a definition of the filtered boundary. In the following we use this definition and denote the filtered domain by $\overline{D}$ and its boundary by $\overline{S}$. Then the direction $\overline{\boldsymbol{n}}$ outward normal to $\overline{S}$ is given by

$$\overline{\boldsymbol{n}} = -\frac{\nabla W}{|\nabla W|} \tag{9}$$

Table 3. Filter shape and size, U_o* is U* of case FS.

filter name	filter shape	filter size Δ_x/H, Δ_y/H, Δ_z/H	filter size in viscous units $\Delta_x U_o^*/\nu$, $\Delta_y U_o^*/\nu$, $\Delta_z U_o^*/\nu$	filter volume $\Delta_x\Delta_y\Delta_z/H^3$
CF1	small cube	0.033, 0.03, 0.033	13, 12, 13	0.0000333
CF2	large cube	0.067, 0.07, 0.067	28, 30, 28	0.000311
PF	planar	0.20, 0.02, 0.133	80, 8, 52	0.000532
SF	spanwise	0.0, 0.0, 0.167	0, 0, 64	(0.0000142)

in the region near boundary where $|\nabla W| > 0$. The definition of W, (7) also indicates that ∇W is the weighted average of the unfiltered normal direction $\boldsymbol{n}$ on the unfiltered boundary S since

$$\begin{aligned}\nabla W &= \nabla \iiint_D w\left(\frac{\xi - x}{\Delta}\right) dV_\xi \\ &= -\iiint_D \nabla_\xi w\left(\frac{\xi - x}{\Delta}\right) dV_\xi \\ &= -W \iint_S G(\boldsymbol{x},\boldsymbol{\xi})\,\boldsymbol{n}\, dS_\xi\end{aligned} \quad . \tag{10}$$

If we use notation

$$\overline{\boldsymbol{n}}^S(\boldsymbol{x}) = \iint_S G(\boldsymbol{x},\boldsymbol{\xi})\,\boldsymbol{n}(\boldsymbol{\xi})\, dS_\xi \,, \tag{11}$$

we see that $\overline{\boldsymbol{n}}$ and $\overline{\boldsymbol{n}}^S$ are parallel and

$$\overline{\boldsymbol{n}} = \overline{\boldsymbol{n}}^S \frac{W}{|\nabla W|} = \frac{\overline{\boldsymbol{n}}^S}{|\overline{\boldsymbol{n}}^S|} \tag{12}$$

which is defined again in the region where $|\nabla W| > 0$.

In the numerical filtering of the DNS results shown in the next section, for the weight function w we use the top-hat function with three different shapes as shown in Table 3. The first two denoted by CF1 and CF2 are a top-hat close to a cube with almost equal sides. The third one denoted by PF is a filter that has small thickness in the direction normal to the boundary but large in the streamwise and the spanwise directions. This corresponds to most numerical grids used in typical LES computations that resolve best in the wall-normal direction but rather coarse in the other directions. The last one SF is a filtering only in the spanwise z direction which often is assumed when some kind of explicit filtering is needed in calculation of flows with two-dimensional mean field. Specifically, filter CF1 and CF2 have sizes (Δ_x/H, Δ_y/H, Δ_z/H) = (0.034, 0.035, 0.034) and (0.067, 0.07, 0.067), respectively, which are roughly cubes of sides 1/26th and 1/13th of the channel height corresponding roughly to filtering by equally-spaced grids of 26 and 13 points, respectively. The first one is smaller than the roughness height which is about 20 viscous lengths in the flat smooth surface case. The latter one is twice as large as the roughness height. Filter PF has the thickness as small as 0.02H but the length and width as large as 0.2H and 0.13H, respectively and the volume is about the same as CF2. Filter SP has zero height and streamwise length but as long as 0.17H in the spanwise direction which is about 1.2 times the roughness wave length.

In the following, the results of the DNS conducted in curvilinear coordinates are first interpolated on uniformly spaced rectangular grid of 180x220x96. Then spatial averaging is performed according to the top-hat filters described above. It is done only every 1000 time steps of the DNS calculation and the time averages are taken over 200 of these samples. Additional averaging in the spanwise direction and/or same phase locations with respect to the boundary geometry are also done to improve convergence of averages.

3.2 Filtering of flow over flat smooth surface

Before applying the filtering defined above to the presently simulated flows over rough surfaces, the same filtering is performed on the better known flow FS over flat smooth surface. First the time averages of the filtered flow are examined. We use the overbar with a single quotation to denote the deviation of the filtered flow from its time average, $\bar{f}' = \bar{f} - \langle \bar{f} \rangle$ so that $-\langle \bar{u}'^2 \rangle$, $-\langle \bar{v}'^2 \rangle$ and $-\langle \bar{u}'\bar{v}' \rangle$ correspond to what are treated as the Reynolds stress components of the resolved flow in a typical LES and are called here the Reynolds stresses of the filtered flow.

The results of the time mean of the filtered streamwise velocity $\langle \bar{u} \rangle$, the Reynolds shear stress $-\langle \bar{u}'\bar{v}' \rangle$ and the normal stresses $\langle \bar{u}'^2 \rangle$ and $\langle \bar{v}'^2 \rangle$ normalized by U*^{2}, of flows filtered with filters CF1, CF2, PF and SF are shown in Figure 16. Since the mean flow changes only in the wall-normal direction, the filtering effects appear for filters with finite thickness in y direction and the spanwise filter SF does not have any effect. It is seen that significant filtering effects appear even on the mean velocity with a filter of thickness $\Delta_y U^*/\nu$ =30 of CF2. It should be noted that the present definition of the filter implies that points below $\Delta_y U^*/\nu$ =15 are influenced by the boundary and the mean filtered velocity does not necessarily is zero at the position of the original boundary.

As to the effects on the turbulent stresses, small cubic filter CF1, which has the viscous scale $\Delta_y U^*/\nu$ of about 13, loses only about 10 percent of the shear stresses at the most, and this filter may be said to resolve the wall layer. Filters PF and SF that may be used in typical practical LES are seen to remove as much as 50 percent of the Reynolds shear stress at about y/H=0.1 that is $yU^*/\nu \approx 40$. The differences between the filtered and the unfiltered stresses are the sub-filter residual contributions and correspond to the time mean of SGS stresses in LES with grid spacing similar to these filter sizes. Grid spacing comparable to the size of these filters is not exceptional in many LES's of high Reynolds number flows, and these results indicate that the modelled subgrid contributions should really be included in the evaluation of results of LES with the resolution of this level. Compared with the effects on the shear stress, the filtering effects on the streamwise normal stress are smaller, and those on the wall-normal stress are larger and over larger region. It implies that there are more small

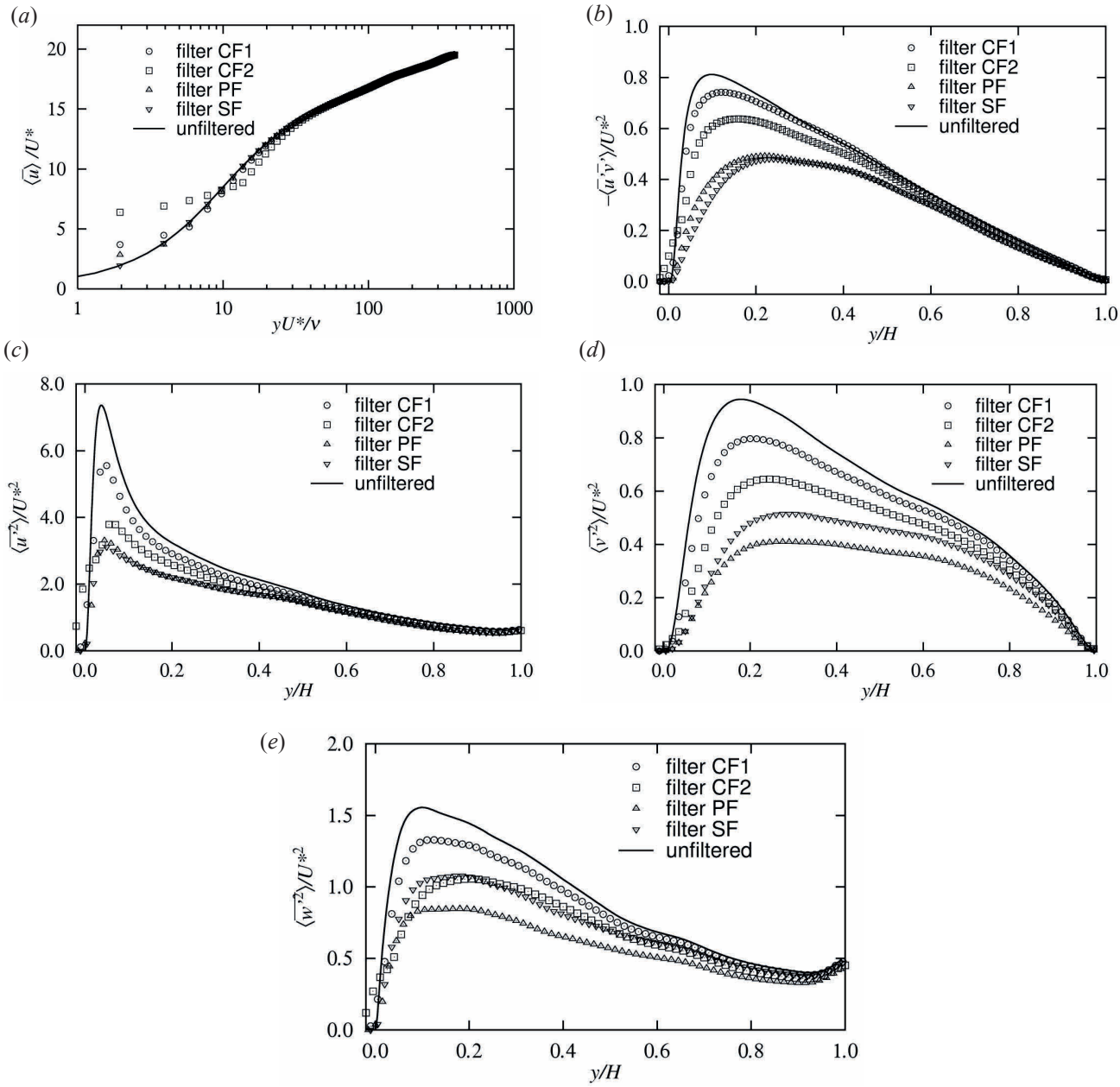

Fig. 16 (*a*) Mean velocity, (*b*) Reynolds shear stress, (*c*) streamwize normal stress, (*d*) wall-normal and (*e*) transverse Reynolds stress of the filtered flow FS over flat smooth surface. ○, filter CF1;□, filter CF2; △, filter PF; ▽, filter SF; —, unfiltered.

scale fluctuations in the wall-normal component than in the streamwise component. Also note that filtering does not shift the peak position of $\langle\bar{u}'^2\rangle$ but the peak positions of $-\langle\bar{u}'\bar{v}'\rangle$ and $\langle\bar{v}'^2\rangle$ move considerably outwards. Although the filtered turbulent kinetic energy is not shown, it is very close to the result of the filtered streamwise normal stress, and filter CF1 is said to resolve more than 80% of the original turbulent energy except at the position of the peak. The other filters retain only about 50 % in most of the inner layer.

In order to see how these filtering effects are related to the characteristics of the large-scale flow, the filtered instantaneous flow structures are shown in Figure 17 for three filters CF2, PF and SF together with the unfiltered flow for reference. Figures 17(*a*), (*c*), (*e*) and (*g*) show distributions of regions of high and low streamwise velocity in plane y/H=0.08, or yU^*/ν=32 in grey scale. This type of plot is often used to visualize streak structures in the inner layer. The facing right-side Figures 17(*b*), (*d*), (*f*) and (*h*) show the surfaces of constant value of the second invariant λ_2 of the velocity gradient tensor for the corresponding cases, that are often used to visualize vortex structures. They also show the magnitudes of the streamwise velocity on wall-normal *x*-*y* and *y*-*z* planes on the far side. The latter is for qualitative information of the distributions by the darkness. The value of λ_2 plotted is $6(U_m/H)^2$ for the unfiltered case (Figure 17(*b*)) and that filtered by CF2 (Figure 17(*d*)) but smaller value of $2(U_m/H)^2$ for those filtered by PF and SF. The results of filter CF1 are between the unfiltered and the CF2 results and not plotted. It is seen that the streak structures are only smeared a little by all filtering leaving much of the structure unchanged but the vortex

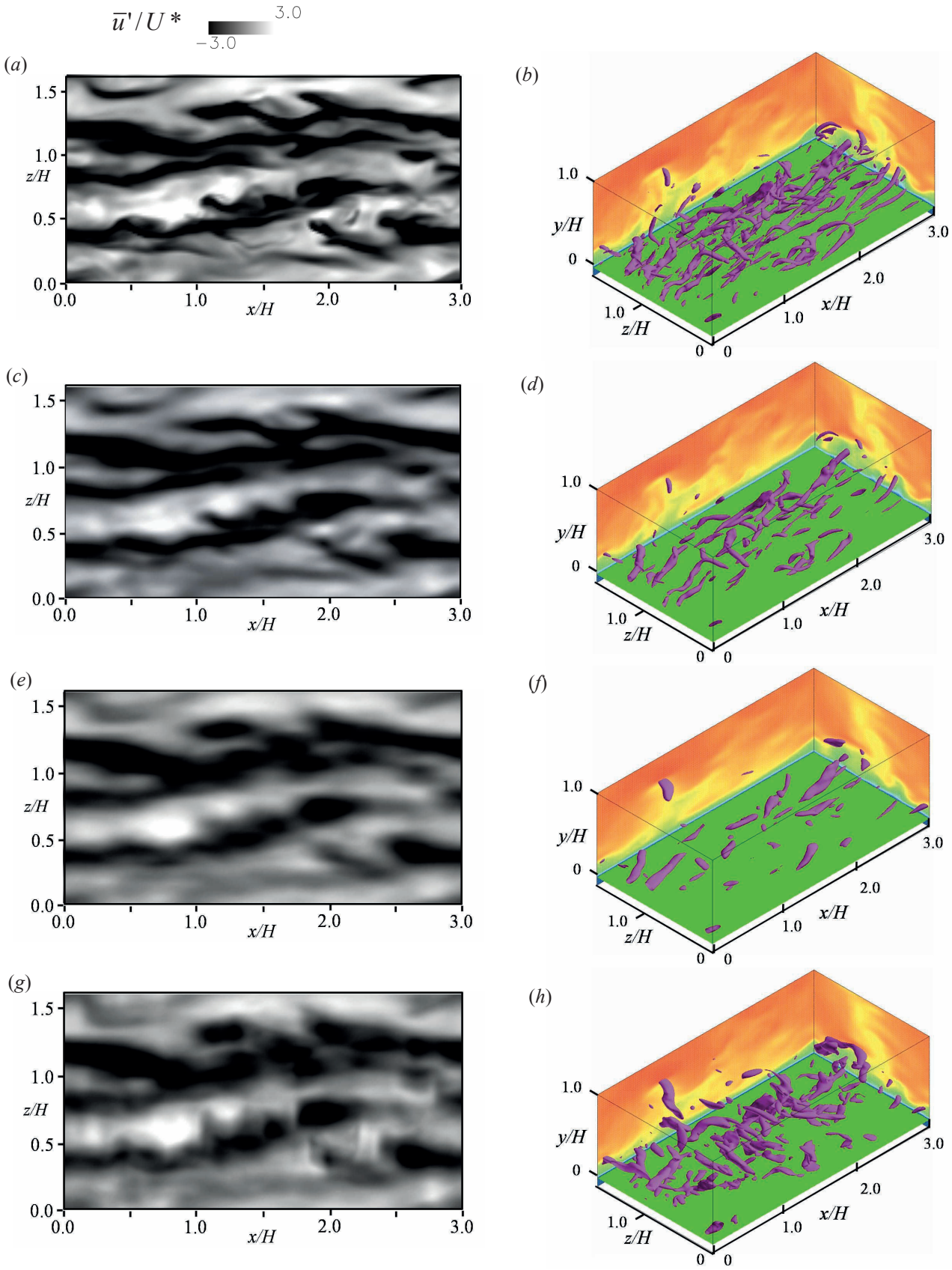

Fig. 17 Distribution at y/H=0.08 of streamwise-velocity fluctuation of (*a*) unfiltered, (*c*) filtered by CF2, (*e*) by PFand (*g*) by SF, and surfaces of constant second invariant λ_2 of velocity gradient tensor (*b*) $6(U_m/H)^2$of unfiltered flow, (*d*) $6(U_m/H)^2$ of flow filtered by CF2, (*f*) $\lambda_2=2(U_m/H)^2$ by PF, and (*h*) $2(U_m/H)^2$ by SF of case FS,

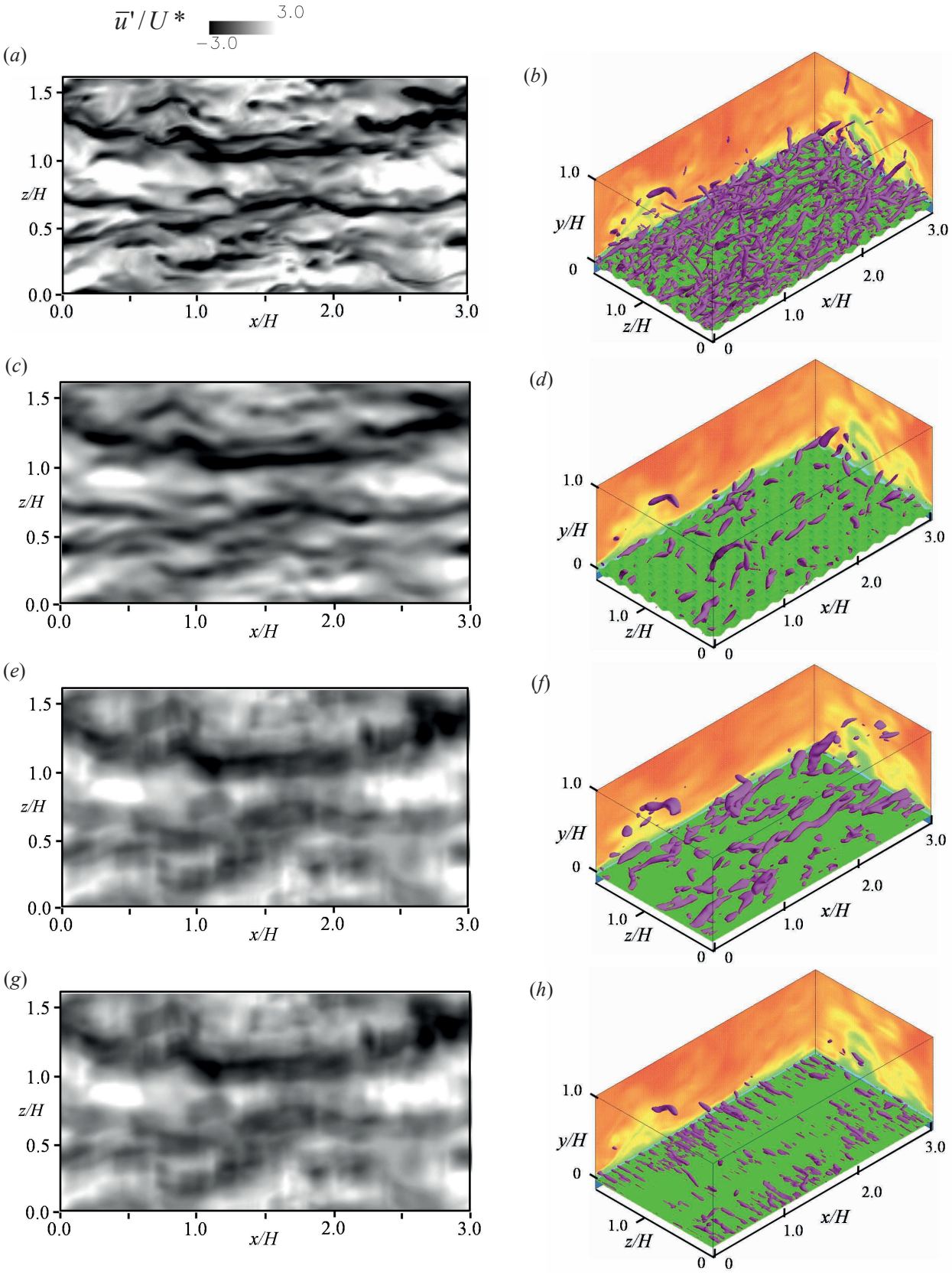

Fig. 18 Distribution at y/H=0.08 of streamwise-velocity fluctuation of (*a*) unfiltered, (*c*) filtered by CF2, (*e*) by PFand (*g*) by SF, and surfaces of constant second invariant λ_2 of velocity gradient tensor (*b*) $6(U_m/H)^2$of unfiltered flow, (*d*) $6(U_m/H)^2$ of flow filtered by CF2, (*f*) $2(U_m/H)^2$ by PF, and (*h*) $8(U_m/H)^2$ by SF of case FR3,

structure indicated by λ_2 iso-surfaces is modified greatly and it depends strongly on the size and the shape of the applied filter. It confirms that the streak structures in the inner layer are of large scales, about three to four streaks in the present simulation region, and are much larger than the sizes of all the filters while the structures indicated by λ_2 iso-surfaces have scales smaller than the widths of the applied filters. Filter CF2, is seen to preserve much of the vortex structures. Plane filter PF also retains the qualitative feature but the scales of the structures are larger and the values of λ_2 are smaller. The spanwise filtering SF alters the qualitative structure completely. It appears that the original vortex structures appear to have length scales in three different directions roughly proportional to the ratios of the filter widths of PF so that PF leaves qualitative shapes but with larger scale. It may be said that the reduction of the turbulent shear stress and the turbulent energy by filtering is related more to losing of the vortex structure than the streak structure. Natrajan & Christensen [43] also showed that the vortex structures are important in energy transfer between the filtered and sub-filter scale flow.

With these characteristics of filtering on smooth-surface flow in mind, we examine the filtered flows of rough and wavy surfaces.

3.3 Instantaneous structure of filtered flows over flat rough surfaces

Here we present similar results of filtering of flow over rough surface case FR3. Figure 18 shows results similar to those shown in Figure 17 for flat rough surface case FR filtered with CF2, PF and SF. The value of λ_2 of the iso-surface for the unfiltered flow is $12(U_m/H)^2$ but the values for those filtered by CF2 and PF are the same as the corresponding cases shown in Figure 17. It should be noted that the bottom boundary in these figures are the filtered boundary as defined by $W=1/2W_m$ and is an indication of the size of the applied filter. It is seen that CF2 smoothes the roughness only slightly but PF and SF reduce the roughness height significantly. Comparing these with the smooth-surface flow results, the structures of the rough surface flow contain significant small-scales both in the streamwise velocity streak structure and the vortex structure. But the filtered results in which small scales are removed, show interesting similarities. Particularly with CF2 and PF, the filtered boundary of the rough surface is almost flat and the filtered rough-surface flows appear not too much different from the corresponding filtered smooth-surface flows. Another interesting result is that filtering in spanwise direction does not remove all the small structures and the SF filtered rough surface flow appears very much different from that of smooth flow. These results indicate that the appropriately filtered flows have similar large-scale strucures as that over smooth surface and partly support the well-accepted interpretation that the roughness increases the resistance and the dissipation but does not alter the large-scale flow structures.

3.4 Time-averaged results of filtered flow over flat rough surfaces

Now the time-averages of the filtered flow over rough surfaces FR2 and FR3 at $x/\Lambda=z/l_z=0$ that is the peak position of the roughness waves are presented. The results at other positions differ only near the boundary and the rest of the distributions are not very different. The mean streamwise velocity $\langle\overline{u}\rangle$, the Reynolds shear stress $-\langle\overline{u}'\overline{v}'\rangle$ and the normal stresses $\langle\overline{u}'^2\rangle$ and $\langle\overline{v}'^2\rangle$ normalized by U^{*2}, of flows filtered with filters CF1, CF2, PF and SF as well as those of the unfiltered flow are shown in Figure 19.

It is first noted that the distributions of the filtered mean velocity, the filtered shear stress and the filtered normal stress show striking similarities with the corresponding filtered quantities of flow over flat smooth surface shown in Figure 16. The filtered velocity profiles of rough surface flows are shifted down by a constant down almost to the filtered surface except the spanwise filter SF has a smoothing effect in the three dimensional roughness case FR3. It should be remembered that the total resistance of R2 is about 40% more than that of FS so the reduction in the filtered shear stress in terms of U_m^2 is much larger in the rough surface cases. The normal stresses of unfiltered rough surface flows are more isotropic than smooth-surface flows and the same trend is preserved in the filtered normal stress distributions. However, the near-wall peak in $\langle\overline{u}'^2\rangle$ of both cases FR2 and FR3 is reduced significantly by all filtering compared with the smooth surface case. Particularly, PF and SF remove the near-wall peak almost completely making the distributions almost flat up to about $y/H=0.2$. This is the region where there are direct effects of the roughness and the filtering effects of boundary. The filters remove the streamwise fluctuation mostly near the roughness elements but the normal fluctuations are reduced across the entire width of the channel. The overall trend that the streamwise fluctuation is attenuated less than the wall-normal fluctuation may be compared with the trend of typical coarse LES that underestimates the wall-normal fluctuation but overestimates the streamwise fluctuation (Henn & Sykes 1999).

Further detail can be seen from the filtered two point correlations. Two point correlation coefficient C_{uu} between $\overline{u}$ at reference point $(x_{ref}, y_{ref}, z_{ref})$ and $\overline{u}$ at a general point (x,y,z) defined by

$$C_{uu}(x,y,z) = \frac{\left\langle \overline{u}(x,y,z,t)\overline{u}(x_{ref},y_{ref},z_{ref},t)\right\rangle}{\sqrt{\left\langle(\overline{u}(x,y,z,t))^2\right\rangle}\sqrt{\left\langle\left(\overline{u}(x_{ref},y_{ref},z_{ref},t)\right)^2\right\rangle}} \tag{13}$$

has been computed for case FR3 and is shown in Figure 20 for the unfiltered flow, and flows filtered by CF2, PF and SF. The contours of constant correlation coefficient are known to be generally concentric ellipses centered around the reference point, and if the reference point is taken in a shear flow, they are inclined from the main flow direction indicating the direction of the dominant structure. In the present case, the reference point is taken at $x/H=1.5$, $y/H=0.08$ or $yU^*/\nu=32$, which is indicated by + in the figure. The contours of $C_{uu}=0.4$ and 0.2 for the unfiltered flow are seen to be inclined about 10 degrees from x direction and extends by about $0.3H$ in the streamwise direction, which is about the same as the measurement by Nakagawa & Hanratty [44]. Generally the presently applied filters do not alter the large-scale characteristics very much, except the contours for filtered flows are larger ellipses and the angle of inclination appears to depend somewhat on the shape of the filter used. The flatter filter gives less inclined contours but not by large amount.

The filtered flow fields over flat rough surfaces examined above indicate that the filtering does extract large structures retaining much of the important characteristics of the dynamics of turbulence by removing small scales and can be a basis for evaluating simulation of large eddies. However, the reduction in turbulent stresses are significant and inclusion and accurate representation of contributions of unresolved motion is important.

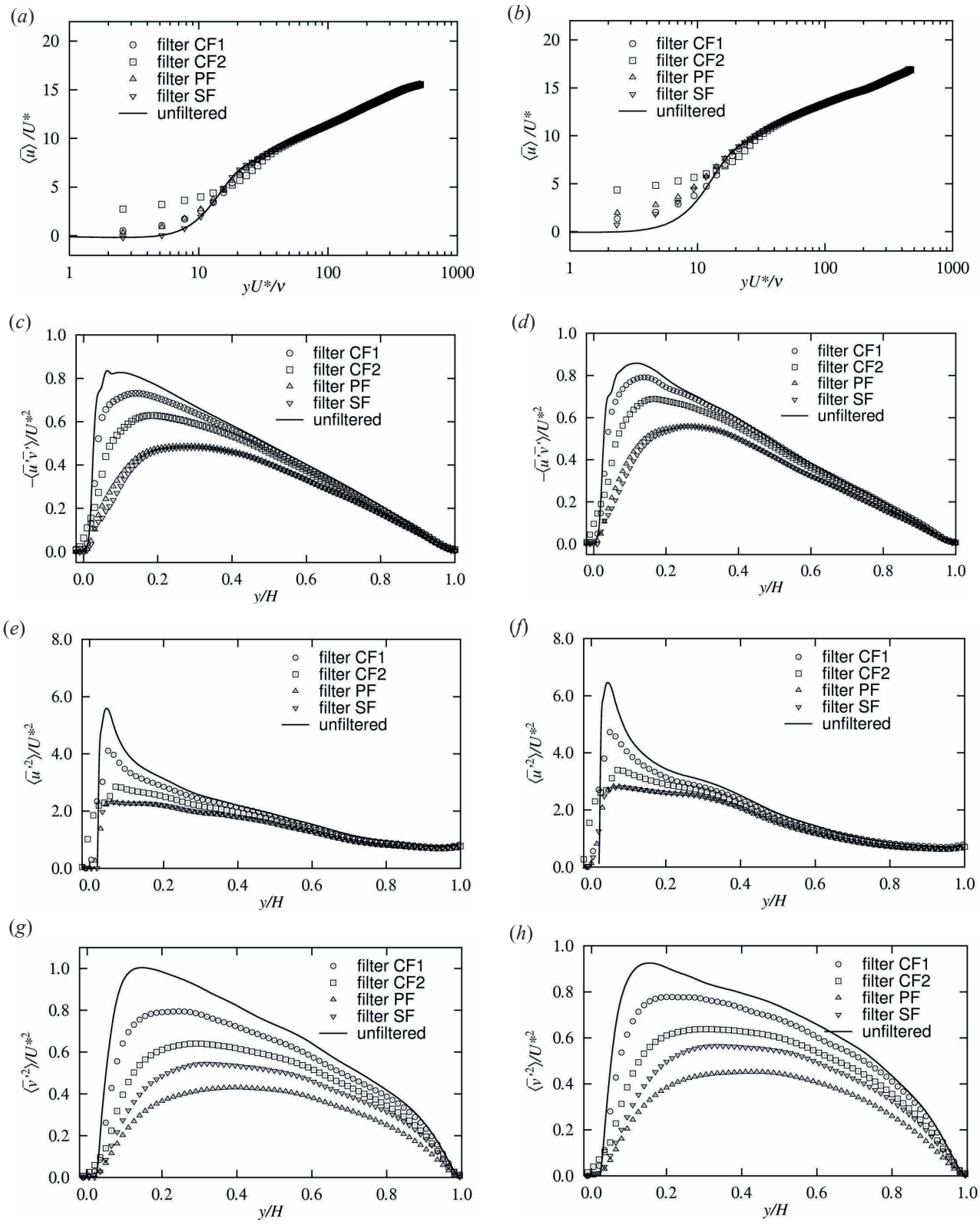

Fig. 19 Mean velocity, Reynolds shear stress and turbulence intensities of the filtered flows over flat rough surfaces, at x/Λ=0, z/l_z=0. (*a*) mean velocity, (*c*) Reynolds shear stress, (*e*)streamwise normal stress, (*g*) wall-normal stress of FR2, and (*b*) mean velocity, (*d*) Reynolds shear stress, (*f*) streamwise normal stress, (*h*) wall-normal stress of flow FR3; ○, filter CF1;□, filter CF2; △, filter PF; ▽, filter SF; —, unfiltered.

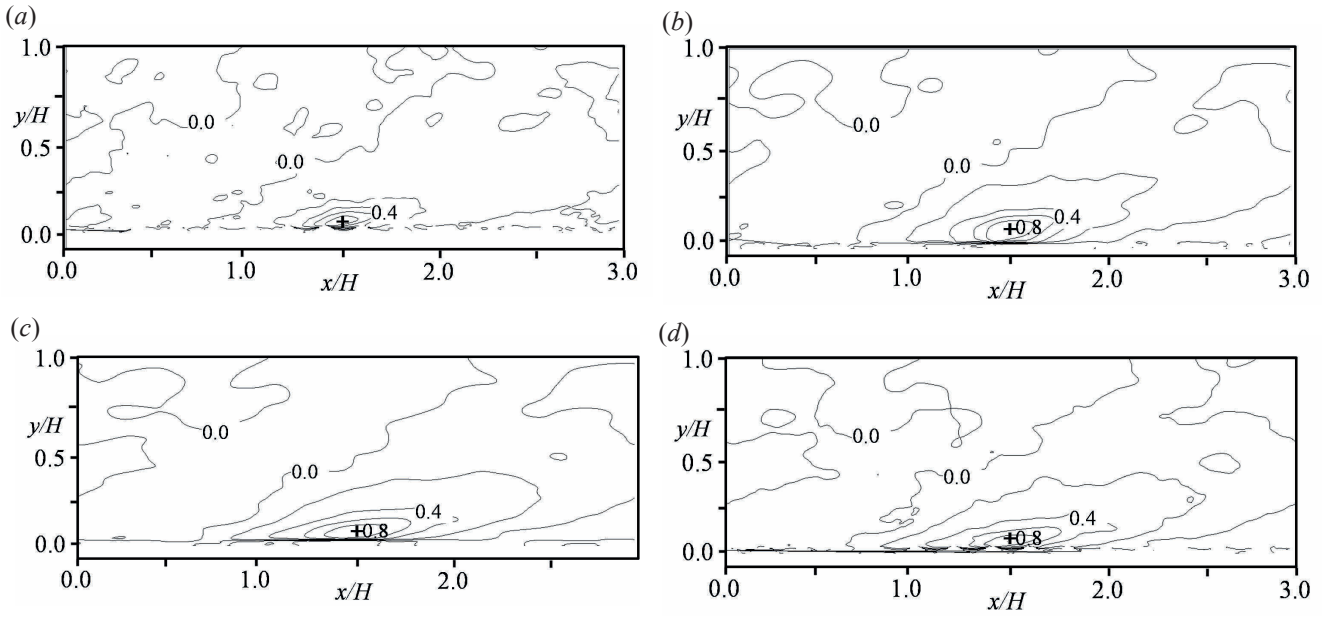

Fig. 20 Two-point correlation C_{uu} between $\overline{u}'(x_{ref}, y_{ref}, z_{ref}, t)$ and $\overline{u}'(x, y, z_{ref}, t)$ in flow WR2. (*a*) unfiltered flow, (*b*) filtered by CF2, (*c*) filtered by PF, and (*d*) by SP, +, (x_{ref}, y_{ref}).

3.5 Instantaneous structure of filtered flow over a wavy rough surface

Next similar filtering described in the previous sections is applied to flows over wavy rough surfaces. Figure 21 shows similar filtered instantaneous vortex structures of case WR3 on the left side and compared with the filtered flows over smooth wavy surface flow of WS on the right side of the same figure. The bottom boundaries of these figures are all filtered boundaries as defined by $W=1/2W_m$. It is seen that the boundary of WR3 filtered by CF2 shows some three dimensional waviness of the roughness but those filtered by PF and SF are seen to have removed the small roughness and the boundaries look about the same as the wavy smooth surface WS shown on the right side. The vortex structure now is very much different from that on the flat surface. Vortices are finer and mostly generated just downstream of the crest of the waviness and disappear at the next crest. The flow with roughness does contain more small scales but not as much as over flat rough surface shown in Figure 17(*a*) and (*b*). Filter CF2 removes these small scales but does not alter the structure very much. Filters PF and SF in particular modify the vortex structure significantly. However, it should be noted that the filtered flow structures of the rough surface flow WR3 and those of the smooth surface SW are quite similar. This is important since it indicates that the small boundary roughness does not greatly modify the filtered flow and that its effects may be modeled like sub-grid scale motion.

Figure 22 shows the streak structure of unfiltered and filtered flow over the wavy rough surface WR3 compared with the corresponding cases of WS. They are on a surface $0.08H$ above the filtered boundary, i.e. at $y/H = 0.08 + \overline{y_W + y_r}$, that corresponds to the plane shown for flat rough surface case FR3 in Figure 18. The streak structures similar to those seen In smooth wavy surface flow (De Angelis et al. [12]) are also seen in the unfiltered wavy smooth flow of case WS with wave crests interfering with the long streaks. The streaks of the rough case WR3 contain considerable small scale fluctuations. The filtering by all filters presently used remove these small-scale fluctuations and the filtered streak structures are remarkably similar to the smooth surface results. These again imply the streak structure is retained fairly well by filtering.

3.6 Time averaged quantities of flows over wavy rough surfaces

Now we examine the filtered rough-surface flows influenced by the streamwise changes of the pressure gradient and the boundary shape from the results of filtered flows over wavy rough surfaces. As shown in Figure 9, the wall pressure increases from the crest of the waviness to the point between the trough and the next crest. It decreases considerably over the crest of the waviness. Figure 23 shows the time averaged velocity vectors and the separation streamline in the bottom half of the basic period of the wavy rough surface flows WR2 and WR3 filtered by CF2 compared with the similarly filtered flow over wavy smooth surface WS. For Case WR3, distributions at two spanwise locations, one in the plane z/l_z=0.0 in which the top of roughness coincides with the peak of the waviness, and the other z/l_z=0.5 along which the bottom of the roughness is at the crest of the waviness, are shown. The flow filtered with the present kernel integral is defined even outside the original or the filtered boundary and it is not zero there. However, it is seen that the separation streamline, which may roughly be thought of the effective boundary for flow in the main channel, is mostly within the flow near the filtered boundary. The streamline in plane z/l_z =0.5 of WR3 goes outside the boundary but the velocity is very small there.

The mean velocity profiles of WR3 filtered by CF2 and PF are plotted in Figure 24(a) and 24(b), respectively and compared with the filtered flow of WS. The profiles are plotted against the distances from the filtered boundary $\overline{y_W + y_r}$. It is seen that the mean velocity profiles filtered by the same filter are similar if plotted against the distance from the filtered boundary, but quite different for different filters. The region up to about y/H=0.4 is the region influenced by the pressure gradient due to the waviness. The width of the filter CF2 is about 1/5 of this layer but the thickness of this layer appears larger than the flow filtered by

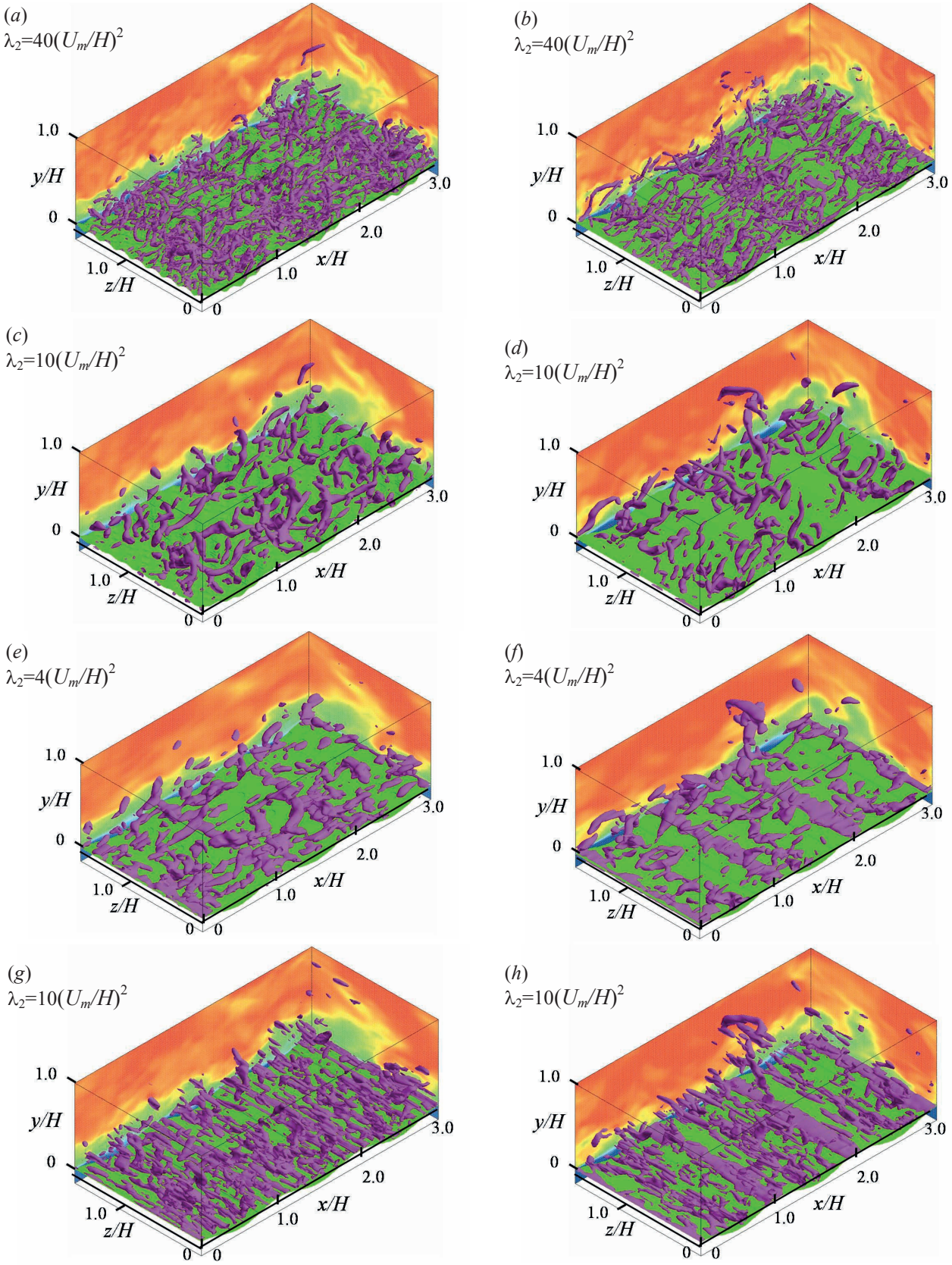

Fig. 21 Instantaneous vortex structure of unfiltered and filtered flows by surfaces of constant λ_2 of (*a*) unfiltered flow, (*c*) filtered by CF2, (*e*) by PF, (*g*) by SF of WR3, and (*b*) unfiltered flow, (*d*) filtered by CF2, (*f*) by PF, (*h*) by SF of SW, $\lambda_2=40(U_m/H)^2$ for (*a*) and (*b*), $\lambda_2=10(U_m/H)^2$ for (*c*), (*d*), (*g*) and (*h*), and $\lambda_2= 4(U_m/H)^2$ for (*e*) and (*f*).

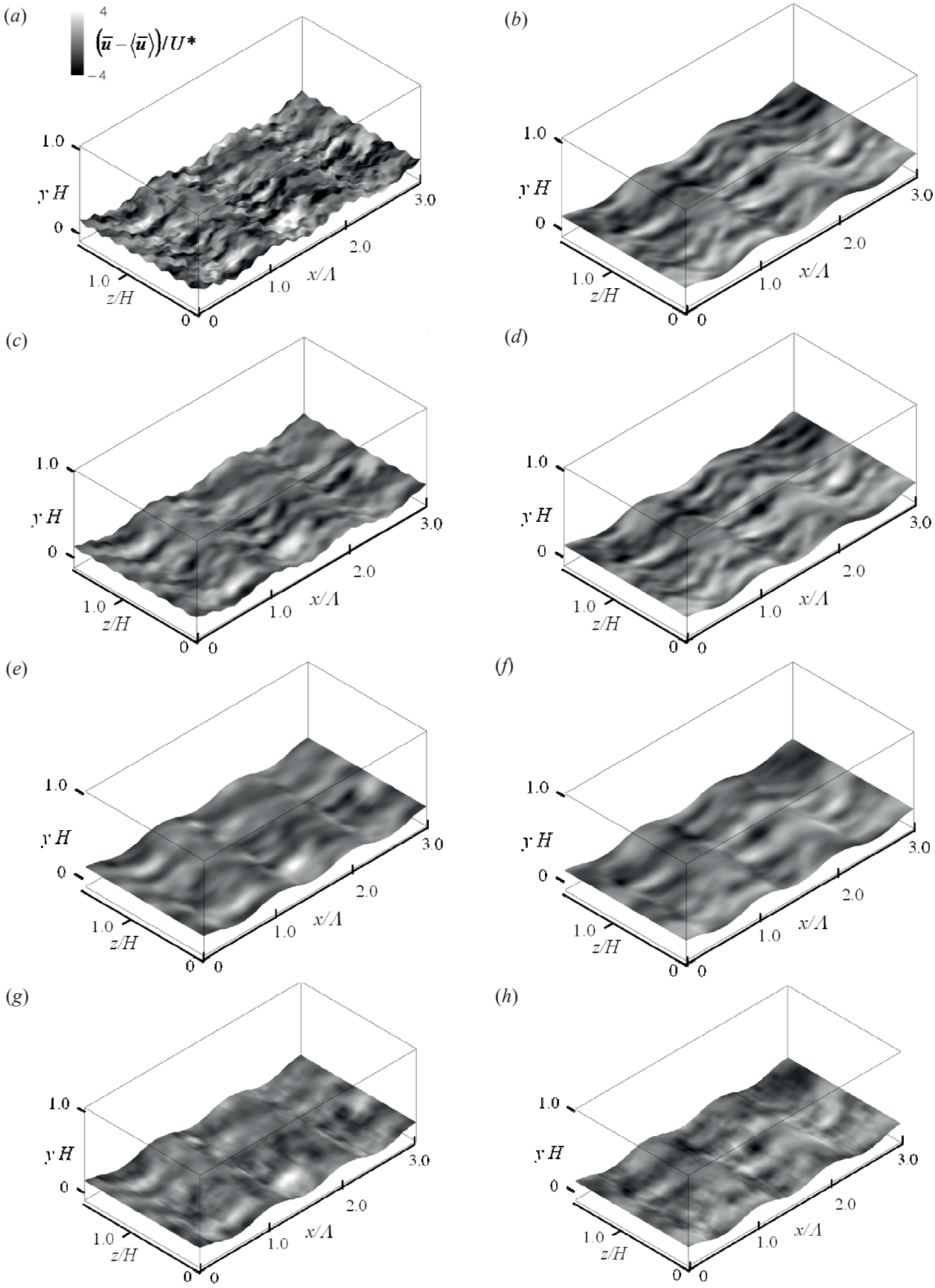

Fig. 22 Instantaneous streak structure of unfiltered and filtered flows of WR3, left column and WS, right column. (*a*), (*b*) unfiltered, (*c*), (*d*) filtered by CF2, (*e*), (*f*) filtered by PF, (*g*), (*h*) by SF, scales are all same.

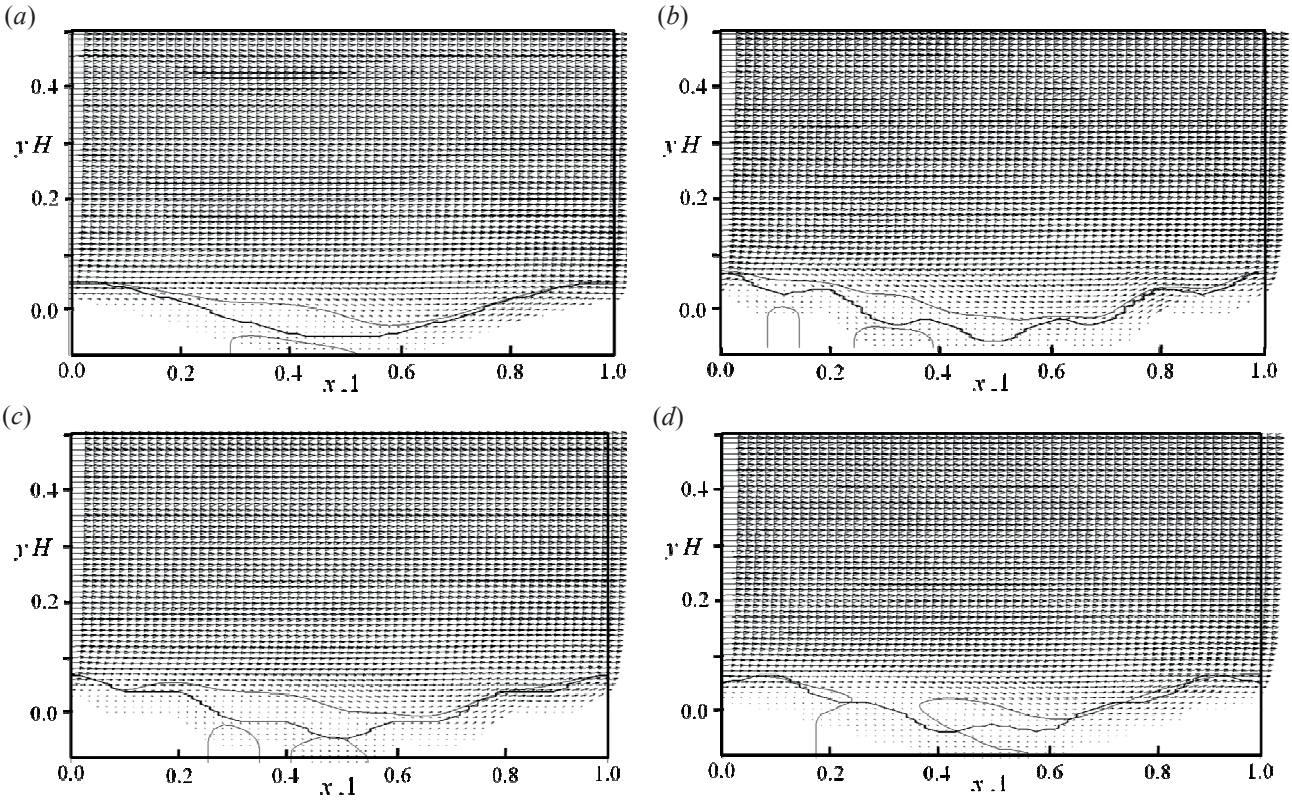

Fig. 23 Mean velocity vectors and the separation streamlines filtered by CF2 in bottom half of center wave of the channel. (*a*) SW, (*b*) WR2, (*c*) WR3, z/l_z=0.0; (d) WR3, z/l_z=0.5.

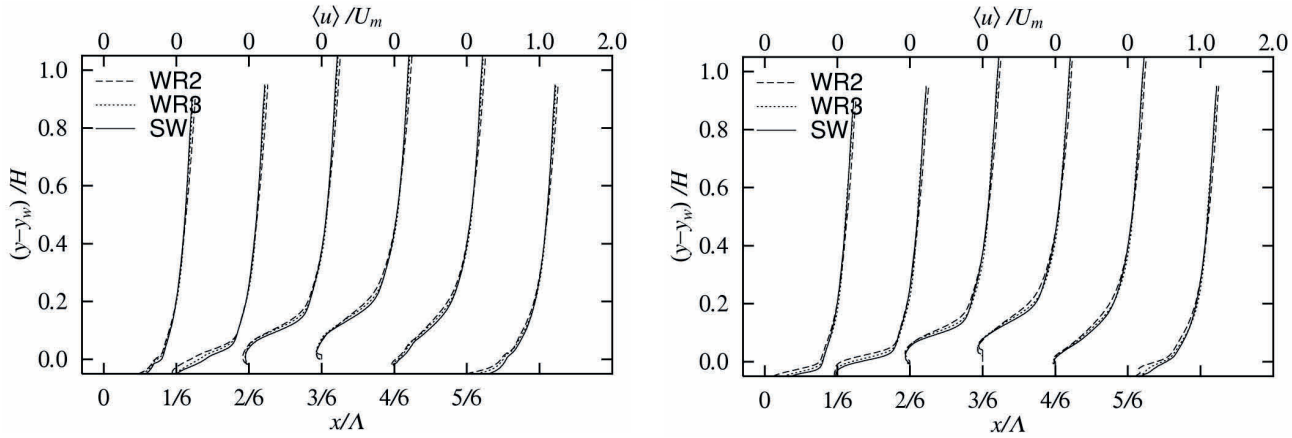

Fig. 24 Filtered mean velocity profiles; (*a*) CF2; (*b*) PF, ____ , SW; _ _ _ _ ,WR2; ..... , WR3.

thinner filter PF. The slope of the velocity implies that the filtered velocity profiles of WR2 and WR3 are smaller than the unfiltered original flows shown in Figure 11 but the filtered flows are similar with or without small roughness.

Figures 25 through 28 show the distributions of the Reynolds stress components normalized by U_m^2 of the filtered flows in the bottom half of the basic period of waviness. Normalization by the bulk scale U_m^2 is chosen since no appropriate local scale is known. The results of filter CF2 are shown as a representative case. These results show the effects of streamwise changes of the pressure gradient and the boundary. It is seen that the Reynolds stresses do reduce by filtering but the shape of distributions does not change much but broadened slightly in the general wall normal direction. The filtered stresses do not become zero on the filtered boundary, shown in thick lines, since they represent the fluctuations in the neighborhood of distances equal to about half of the filter width. This is another result and a purpose of filtering. With filter CF2, either in the smooth case WS or rough cases WR2 and WR3, the local undulations of contour curves are smoothed and there is little region of negative shear stress, on the upslope surface of individual roughness waves. The filtered results of WR2 and WR3 are now quite similar to the filtered smooth case WS. Besides the large-scale structures of the turbulent stresses, such as the high shear downstream of the main crest, large $\langle \overline{u}'^2 \rangle$ fluctuation above the trough, $\langle \overline{v}'^2 \rangle$ peaks slightly downstream and large spanwise $\langle \overline{w}'^2 \rangle$ fluctuation on the upslope of the main

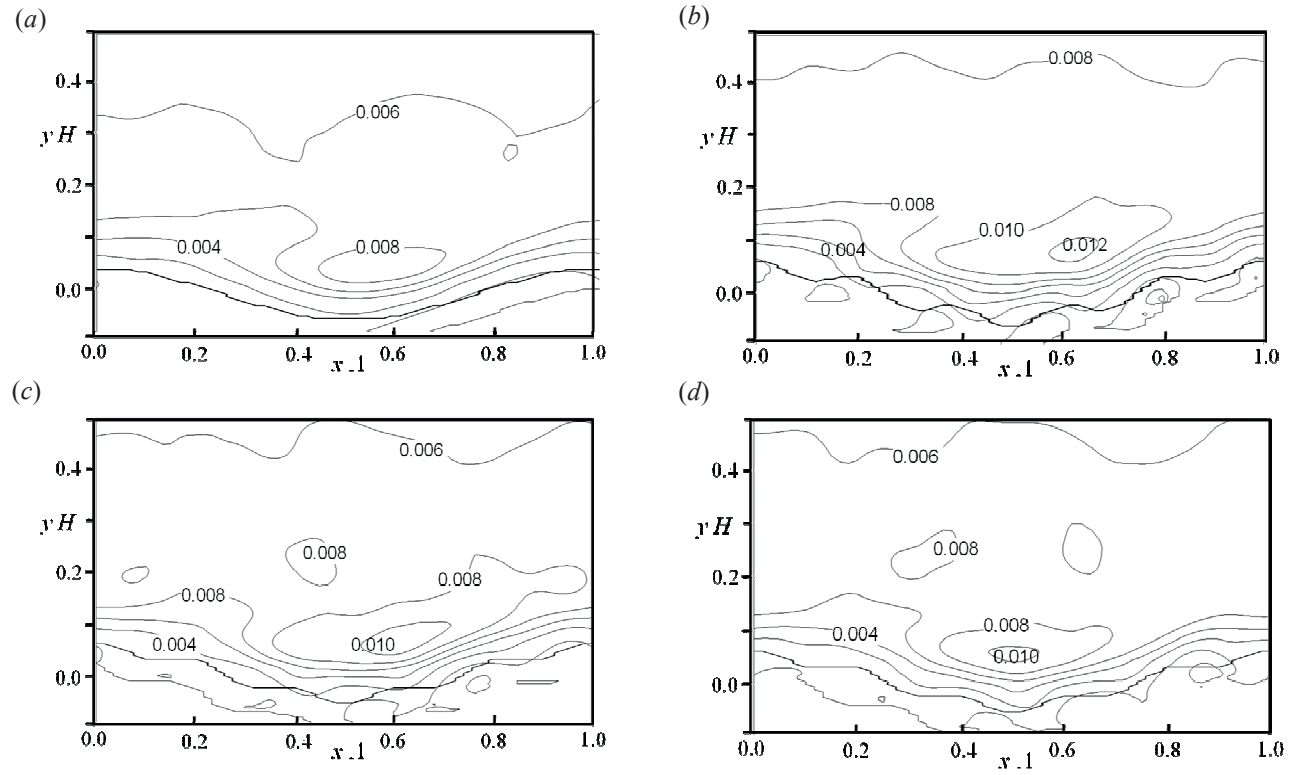

Fig. 25 Reynolds shear stress $-\langle \overline{u}'\overline{v}' \rangle$ normalized by U_m^2 of flows. (*a*) WS, (*b*) WR2, (*c*) WR3 at z/l_z=0.0 and (*d*) WR3 at z/l_z=0.5 filtered by CF2.

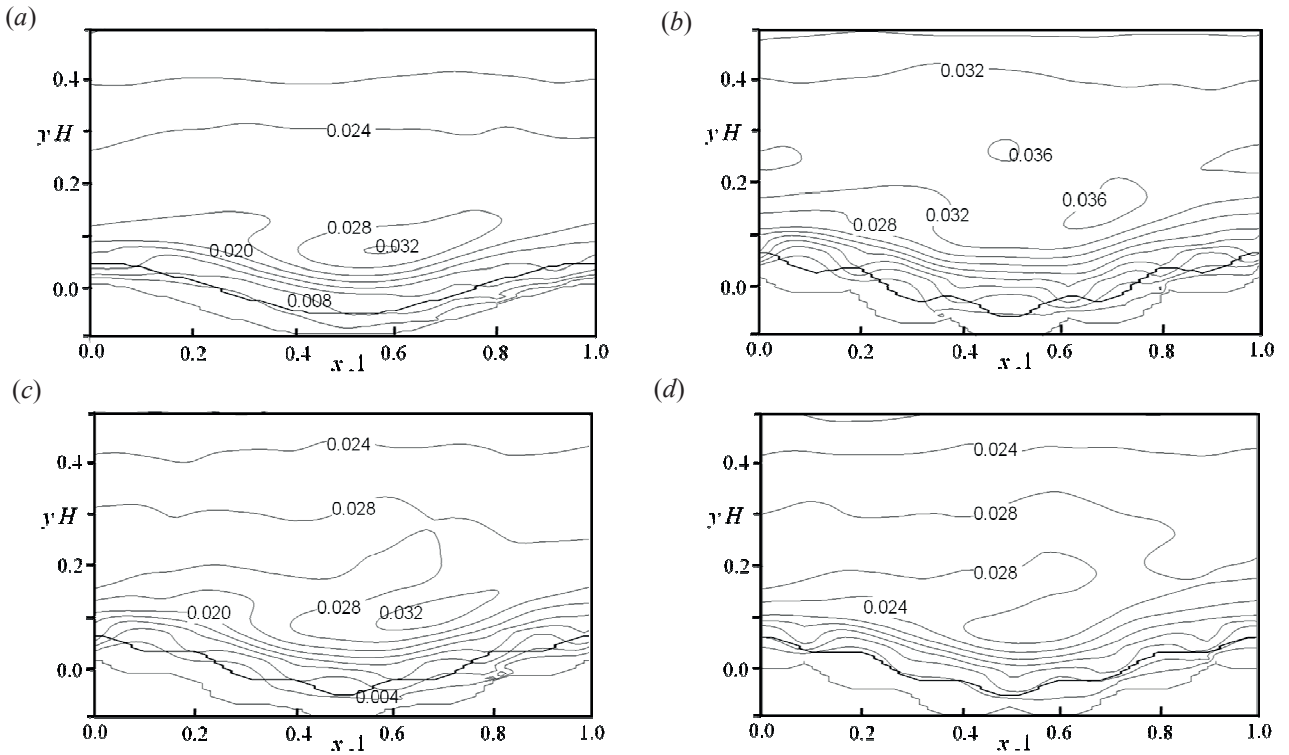

Fig. 26 Reynolds normal stress $\langle \overline{u}'^2 \rangle$ normalized by U_m^2 of flows. (*a*) WS, (*b*) WR2, (*c*) WR3 at z/l_z=0.0 and (*d*) WR3 at z/l_z=0.5 filtered by CF2.

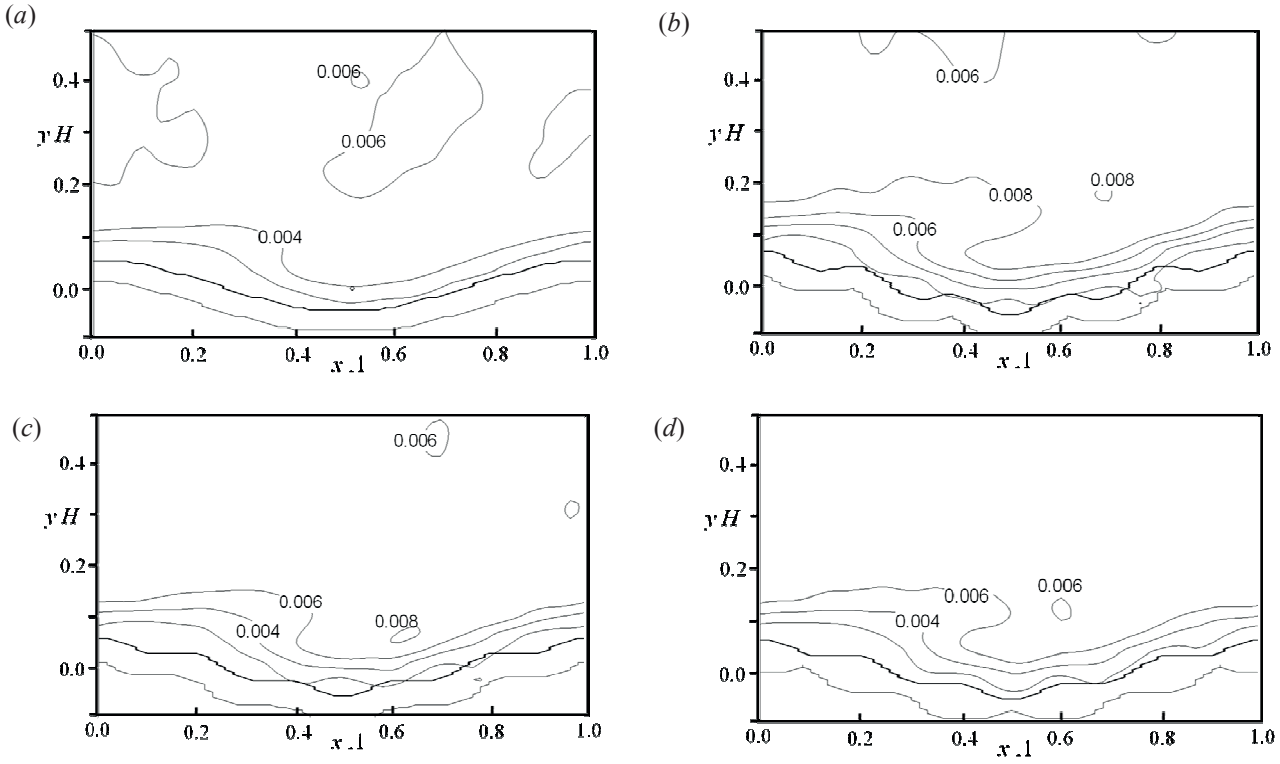

Fig. 27 Reynolds normal stress $\left\langle \overline{v}'^2 \right\rangle$ normalized by U_m^2 of flows. (*a*) WS, (*b*) WR2, (*c*) WR3 at z/l_z=0.0 and (*d*) WR3 at z/l_z=0.5 filtered by CF2.

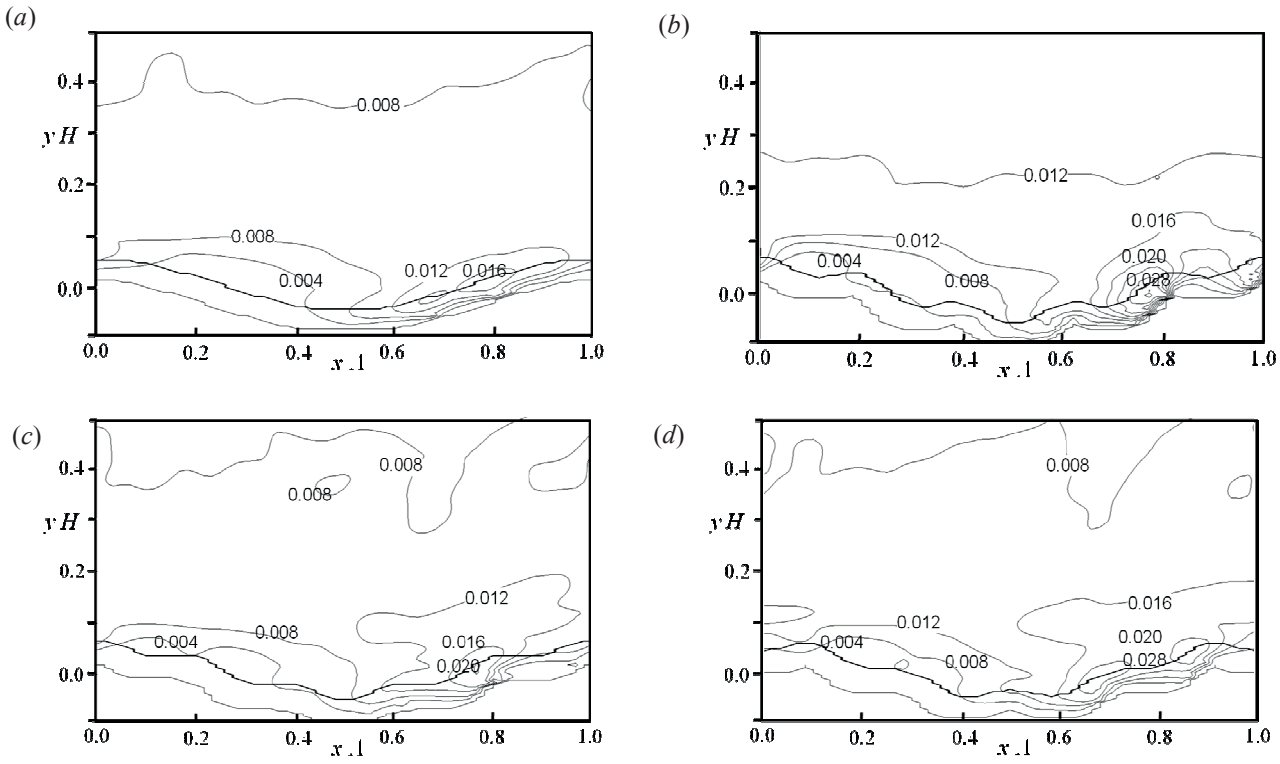

Fig. 28 Reynolds normal stress $\left\langle \overline{w}'^2 \right\rangle$ normalized by U_m^2 of flows. (*a*) WS, (*b*) WR2, (*c*) WR3 at z/l_z=0.0 and (*d*) WR3 at z/l_z=0.5 filtered by CF2.

waviness are all retained with slightly flattened shape of distributions.

The filtered flow characteristics shown above may not be quite the same as the original flow but they do show up the important large structure and if they are to be reproduced by numerical methods with limited resolution which is possible, equations governing them are of interest. We will derive the equations that govern these filtered flow quantities.

4. Equations of motion for the filtered flow.

The filtered flows have been seen to represent large structures characterizing dynamics of the rough- surface flows fairly well for appropriate filter shapes. Although the turbulence energy is reduced considerably they are more amenable to numerical simulations with practical grid sizes. Since they are obtained by explicitly filtering the simulation results, the equations governing them can also be obtained by the same filtering. Here we apply the same filtering that has been used in the previous section to the equations of motion. This will lead to the exact equations that the filtered flow fields satisfy.

We first note that the filter of the divergence of a vector $\boldsymbol{f}$ can be written as

$$\begin{aligned}
\overline{\nabla \boldsymbol{f}(\boldsymbol{x})} &= \iiint_D G(\boldsymbol{x},\boldsymbol{\xi})\, \nabla_\xi \boldsymbol{f}(\boldsymbol{\xi})\, d\xi \\
&= -\iiint_D \nabla_\xi G(\boldsymbol{x},\boldsymbol{\xi})\boldsymbol{f}(\boldsymbol{\xi})\, d\xi + \iint_S G(\boldsymbol{x},\boldsymbol{\xi})\boldsymbol{f}(\boldsymbol{\xi})\boldsymbol{n}(\boldsymbol{\xi})\, dS_\xi \\
&= \iiint_D \left(\nabla_x G(x,\boldsymbol{\xi}) + \frac{\nabla_x W}{W} G \right) \boldsymbol{f}(\boldsymbol{\xi})\, d\xi + \\
&\quad \iint_S G(\boldsymbol{x},\boldsymbol{\xi})\boldsymbol{f}(\boldsymbol{\xi})\boldsymbol{n}(\boldsymbol{\xi})\, dS_\xi \\
&= \iiint_D \nabla_x G(\boldsymbol{x},\boldsymbol{\xi})\boldsymbol{f}(\boldsymbol{\xi}) d\xi - \\
&\quad \iiint_D G(\boldsymbol{x},\boldsymbol{\xi})\boldsymbol{f}(\boldsymbol{\xi})\, d\xi \iint_S G(\boldsymbol{x},\boldsymbol{\xi})\boldsymbol{n} dS_\xi + \iint_S G(\boldsymbol{x},\boldsymbol{\xi})\boldsymbol{f}(\boldsymbol{\xi})\boldsymbol{n}\, dS_\xi \\
&= \nabla \overline{\boldsymbol{f}} + \overline{\boldsymbol{f}\boldsymbol{n}}^{\boldsymbol{S}} - \overline{\boldsymbol{f}}\,\overline{\boldsymbol{n}}^{\boldsymbol{S}} \\
&= \nabla \overline{\boldsymbol{f}} + \overline{\boldsymbol{f}''\boldsymbol{n}}^{\boldsymbol{S}}
\end{aligned} \tag{14}$$

Here $\boldsymbol{f}'' = \boldsymbol{f} - \overline{\boldsymbol{f}}$ is the sub-filter fluctuation and the overbar with superscript S means the weighted integral over the flow boundary

$$\overline{\boldsymbol{f}\boldsymbol{n}}^{\boldsymbol{S}}(\boldsymbol{x}) = \iint_S G(\boldsymbol{x},\boldsymbol{\xi})\boldsymbol{f}(\boldsymbol{\xi})\boldsymbol{n}\, dS_\xi \ . \tag{15}$$

which is a generalization of the definition given by Eq.(11). In the fourth line of this equation, W is expressed in terms of the integral of G. Similar relations have been used in the spatial averaging of flows in complex porous medi
a in which case w=1, and W=V, the volume of the entire flow domain D (Witaker [45] ; Gray & Lee [46]).

Using this relation, the continuity equation

$$\nabla \cdot \boldsymbol{u} = 0 \tag{16}$$

is filtered as

$$\nabla \cdot \overline{\boldsymbol{u}} = \overline{\boldsymbol{u}} \cdot \overline{\boldsymbol{n}}^{S} \tag{17}$$

and the equation of motion

$$\frac{\partial \boldsymbol{u}}{\partial t} + \nabla \cdot (\boldsymbol{u}\boldsymbol{u}) = \nabla \cdot \left(-\frac{p}{\rho}\boldsymbol{I} + \frac{\boldsymbol{\tau}}{\rho} \right) \ , \tag{18}$$

where p is the pressure and $\boldsymbol{\tau}$ is the viscous stress tensor, $\boldsymbol{\tau} = \mu\left(\nabla \boldsymbol{u} + (\nabla \boldsymbol{u})^T\right)$, is filtered to

$$\begin{aligned}
\frac{\partial \overline{\boldsymbol{u}}}{\partial t} + \nabla \cdot (\overline{\boldsymbol{u}}\,\overline{\boldsymbol{u}}) &= \frac{1}{\rho}\nabla \cdot \left(-\overline{p}\boldsymbol{I} + \overline{\boldsymbol{\tau}} \right) - \nabla \cdot \left(\overline{\boldsymbol{u}\boldsymbol{u}} - \overline{\boldsymbol{u}}\,\overline{\boldsymbol{u}} \right) \\
&\quad - \overline{(\boldsymbol{u}\boldsymbol{u})'' \cdot \boldsymbol{n}}^{S} - \frac{1}{\rho}\overline{p''\boldsymbol{n}}^{S} + \frac{1}{\rho}\overline{\boldsymbol{\tau}'' \cdot \boldsymbol{n}}^{S}
\end{aligned} \tag{19}$$

Eq.(17) implies that the velocity near the boundary where $\overline{\boldsymbol{n}}^{S}$ is not zero and does not satisfy the zero-divergence condition. The first line of Eq.(19) is the same as the conventional LES equations of motion, except the filtered viscous stress term $\overline{\tau}$ in $\boldsymbol{\tau}'' = \boldsymbol{\tau} - \overline{\boldsymbol{\tau}}$ of the last term in the second line is the result of filtering of spatial gradient of the velocity, which contains the boundary integral terms as

$$\begin{aligned}
\frac{1}{\rho}\overline{\boldsymbol{\tau}} &= \nu\overline{\left(\nabla \boldsymbol{u} + (\nabla \boldsymbol{u})^T\right)} = \nu\left(\nabla \overline{\boldsymbol{u}} + (\nabla \overline{\boldsymbol{u}})^T\right) + \\
&\quad \nu(\overline{\boldsymbol{u}}\,\overline{\boldsymbol{n}}^{S} + \overline{\boldsymbol{n}}^{S}\overline{\boldsymbol{u}})
\end{aligned} \tag{20}$$

Therefore Eq.(19) can be rearranged to

$$\begin{aligned}
\frac{\partial \overline{\boldsymbol{u}}}{\partial t} + \nabla \cdot (\overline{\boldsymbol{u}}\,\overline{\boldsymbol{u}}) &= \nabla \cdot \left(-\frac{\overline{p}}{\rho}\boldsymbol{I} + \nu\left(\nabla \overline{\boldsymbol{u}} + (\nabla \overline{\boldsymbol{u}})^T\right) + \boldsymbol{R} \right) \\
&\quad + \boldsymbol{U}_S - \frac{\boldsymbol{P}_S}{\rho} + \frac{\boldsymbol{T}_S}{\rho} + \frac{1}{\rho}\nabla \cdot \boldsymbol{\tau}_S
\end{aligned} \tag{21}$$

where

$$\boldsymbol{R} = -\left(\overline{\boldsymbol{u}\boldsymbol{u}} - \overline{\boldsymbol{u}}\,\overline{\boldsymbol{u}}\right) \tag{22}$$

is the sub-filter residual stress tensor, or the usual sub-grid scale terms in LES, and the first three terms in the second line of Eq.(21)

$$\begin{aligned}
\boldsymbol{U}_S &= -\overline{(\boldsymbol{u}\boldsymbol{u})'' \cdot \boldsymbol{n}}^{S} = \overline{\boldsymbol{u}\boldsymbol{u}} \cdot \overline{\boldsymbol{n}}^{\boldsymbol{S}}, \\
\boldsymbol{P}_S &= \overline{p''\boldsymbol{n}}^{S} = \overline{p\boldsymbol{n}}^{S} - \overline{p}\,\overline{\boldsymbol{n}}^{S} \\
\boldsymbol{T}_S &= \overline{\boldsymbol{\tau}''\cdot\boldsymbol{n}}^{S} = \overline{\boldsymbol{\tau}\cdot\boldsymbol{n}}^{S} - \overline{\boldsymbol{\tau}}\cdot\overline{\boldsymbol{n}}^{\boldsymbol{S}}
\end{aligned} \tag{23}$$

are additional body force terms and

$$\frac{1}{\rho}\boldsymbol{\tau}_S = \nu\left(\overline{\boldsymbol{u}}\,\overline{\boldsymbol{n}}^{S} + \overline{\boldsymbol{n}}^{S}\overline{\boldsymbol{u}}\right) \ , \tag{24}$$

is an additional viscous stress which are all the result of interference of the boundary. We will refer the surface integral terms in Eqs.(23) and (24) as the sub-filter boundary terms. Eqs.(17) and (21) describe the motion of the filtered flow, but the right-hand side of Eq.(17) and the terms in the second line of Eq.(21) are due to unresolved boundary and will have to be modelled. Added terms due to boundary surface in near-wall flow were modeled by Bhattacharya et al. [42] but in slightly different forms. The present authors (Nakayama, Hori & Street [47]) also tried modelling of these terms. It is noted

that similar added terms in moving boundary of a free surface have been studied by Shen & Yue [48] and Hodges & Street [49].

Before actually implementing such a method, we will examine from the presently obtained DNS data what the contributions and the roles of these terms are. We note that all added boundary terms other than the last term in Eq.(21) are in the form of body force meaning that they are sources and sinks of momentum. It means that the filtered velocity field does not satisfy the same conservation laws as the unfiltered flow. However, as we will see that they have significant values only in the vicinity of the boundary within distances comparable to the width of the applied filter. It may then be better interpreted as the boundary forces acting on the filtered smooth boundary. Therefore we integrate the added body forces in the direction normal to the filtered boundary, and define

$$\boldsymbol{R}_U = \int_0^{>\Delta_n} (\boldsymbol{U}_S) d\overline{n} \quad , \tag{25}$$

$$\boldsymbol{R}_p = -\frac{1}{\rho} \int_0^{>\Delta_n} \boldsymbol{P}_S \, d\overline{n} \quad , \tag{26}$$

$$\boldsymbol{R}_f = \frac{1}{\rho} \int_0^{>\Delta_n} (\boldsymbol{T}_S + \boldsymbol{\tau}_S \cdot \boldsymbol{n}) d\overline{n} \, . \tag{27}$$

where $\overline{n}$ is the normal distance from the filtered boundary, the upper limit of the integration $>\Delta_n$ is the distance larger than the width of the filter in $\overline{n}$ direction. $\boldsymbol{R}_U$, $\boldsymbol{R}_p$ and $\boldsymbol{R}_f$ are resistance per unit area on the boundary $y = \overline{y_W + y_r}$ due to sub-filter velocity fluctuations, pressure variation and the sub-filter viscous stress, respectively. They balance with the overall pressure gradient and the sum $\boldsymbol{R}_U+\boldsymbol{R}_p+\boldsymbol{R}_f$ may be interpreted as the local resistance.

In the following, as a step towards modelling these sub-filter surface terms, we examine the magnitudes and other properties of them by computing them from the presently obtained DNS data and study the role of these terms and indications as to how they may be modeled.

5. Sub-filter stress and sub-filter boundary terms

First, the filtered velocity components on the filtered boundary are shown in Figures 29 and 30 for cases FR3 and WR3, respectively, together with the filtered boundary $\overline{y_W + y_r}$ defined by the position where W=1/2W_m. These are the instantaneous velocity components $\overline{u}_n$ normal and $\overline{u}_t$ tangent to the filtered boundary in a x-y plane at z=0 at the same instant as the instantaneous data shown in Figures 18 and 21 are taken. The filters used are CF2 and PF. The velocity components filtered by CF2 which has the width about the same as the height of the roughness, contain variations due to the individual roughness waves but those filtered by wider filter PF smoothes the FR3 to almost smooth plane and WR3 to a smooth waviness do not contain fluctuations related to the individual roughness. Generally the tangential component is large at the peak of the smoothed boundary but the normal velocity component is seen to be quite small. Although not exact, it can be said that the zero normal or no-leak boundary condition is a good approximation for both cases.

Next the sub-filter boundary terms are shown in Figures 31 and 32 for cases FR3 and WR3 compared with the conventional SGS stress terms as reference. These are the instantaneous data in plane z=1/2B taken at the same instant as the other instantaneous data are shown. The x-components Us_x, Ps_x and Ts_x of $\boldsymbol{Us}$, $\boldsymbol{Ps}$ and $\boldsymbol{Ts}$, respectively, and the divergence of the x components of the stresses $\boldsymbol{R}$ and $\boldsymbol{\tau}_s$ are shown in the way they appear in the x-component equation of motion. It is noted that for a smooth surface where $\boldsymbol{n}$ is constant and negative of $\boldsymbol{j}$, the unit vector in y direction, $\overline{\boldsymbol{n}}^S = -\boldsymbol{j}$, in which case the pressure integral term $\boldsymbol{P}_S$ vanishes. For comparison, the same gray-scale is used for all plots. The sub-filter boundary terms have non-zero values only near the boundary within distances about half the width of the filter from the actual boundary. Since CF2 has the largest width in y-direction and the region where these terms are not zero is widest. The usual SGS stress $\boldsymbol{R}$ does have large values near the boundary but varies with spatial scale comparable to the filter width and generally negative on the upslope. It does not sharply drop to zero near the boundary but seems to balance with the boundary inertia term $\boldsymbol{U}_S$ and they may better be interpreted together. The pressure integral term P_{Sx} is seen to take mostly negative values in FR3 case and mostly negative in WR3 case except in the reverse-flow region at the trough of the waviness. It indicates that it works mostly as resistance. The viscous-stress integral term T_{Sx}, however, is seen to be positive on the upslope and acts to reduce the resistance there. The magnitude of the viscous stress div$\boldsymbol{\tau}_{Sx}$ is seen smaller than other terms and mostly negative.

As explained in the previous section that these boundary terms act only in a thin layer, they are better interpreted as a boundary resistance. The tangential components particularly are interpreted as the local resistance per unit area. Therefore the components of these forces R_{Ut}, R_{pt} and R_{ft} tangent to the filtered boundary are plotted in Figures 33 and 34 again for cases FR3 and WR3, respectively. These quantities are now non-dimensionalized by the total resistance U^{*2}, since their total balances with the applied pressure gradient. The negative values mean the force opposite the flow direction. It is seen that these resistance terms vary with the scale of the applied filter and is generally negative on the upslope portion of the smoothed boundary. For the filter CF2, the roughness length and the filter width are about the same and large changes with this length scale are seen. As seen in the plots of the stresses in Figures 31 and 32 the conventional SGS stress at the smoothed boundary tends to balance R_{Ut}. For larger filter width in the streamwise direction of PF, the spatial variation is also of this scale. So these resistances are related to the filter scale and the magnitude of the local filtered velocity.

6. Conclusions

Flows over flat and wavy surfaces roughened with two-dimensional and three-dimensional sinusoidal roughness have been simulated by a DNS method and the details of the simulated flows and the large-scale flows obtained by numerical filtering have been studied in detail. With the height of the small roughness waves of 4 percent of the channel height and the roughness Reynolds number of about 20, the properties of the mean velocity and the turbulent stresses of the simulated flows over flat bed are confirmed consistent with existing results of rough surface flows in transitionally-rough range. The simulation results of flows over these roughness waves placed on wavy bed give basic data of effects of pressure gradients and flow separation on rough-surface flows. The large-scale features of these flows extracted by numerical filtering, have then been studied in detail. The filters used correspond to those often assumed in LES of practical large

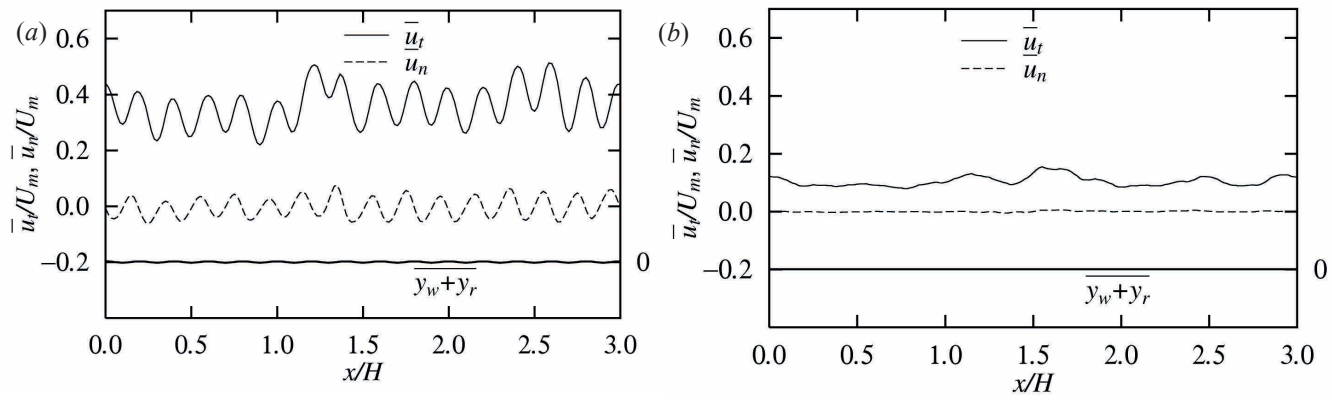

Fig. 29 Instantaneous filtered velocity components, normal $\overline{u}_n$, and tangent $\overline{u}_t$ to the filtered boundary of FR3 at z/l_z=0.25. (*a*) filter CF2 , (*b*) filter PF, ——, $\overline{u}_t$; - - - - , $\overline{u}_n$.

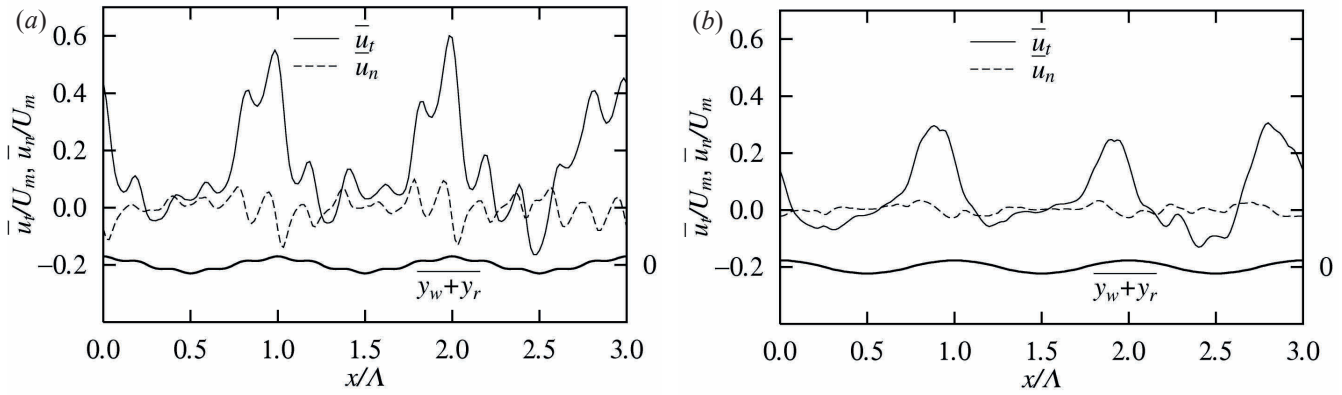

Fig. 30 Instantaneous filtered velocity components, normal $\overline{u}_n$, and tangent $\overline{u}_t$ to the filtered boundary of WR3 at z/l_z=0.25. (*a*) filter CF2 , (*b*) filter PF, ——, $\overline{u}_t$; - - - - , $\overline{u}_n$.

Reynolds number flows, but the effects of the boundary and the filtering of the boundary are also taken into account by using a normalized kernel filter.

The filtered flows over rough surfaces do represent large-scale structures that are important and characterize the entire flow with removed small sub-filter scale effects as added resistance. The sub-filter stresses when filters of sizes and shapes that are likely to be assumed in typical LES of large-Reynolds number flows, are surprisingly large. About 50 percent of turbulence energy is lost by a cubic filter of size about 30 viscous units in the inner layer. A flat filter that resolves better in the wall-normal direction than streamwise or spanwise directions can distort the filtered large structure. The structures of instantaneous filtered flow are strongly depended on the size and the shape of the filters used. The spanwise filtering can completely destroy the important characteristics of the original flow. However, the filtered flows do represent corresponding large-scale flows but the effects of removed small scales are generally large and simulations with grid resolution comparable the presently investigated filter sizes will not give good estimates of turbulence quantities without taking into account the contributions of sub-filter contributions.The exact form of the sub-filter effects have been obtained by filtering the equations of motion when a normalized kernel filter is used. This filter is not uniform but smoothes the flow and the flow field that makes approximate analysis and interpretation of the complex flow possible. The sub-filter boundary effects near solid boundary are identified as the momentum transfer by sub-filter fluctuations, the sub-filter pressure forces and the sub-filter viscous forces. These quantities have been obtained from the simulated results and examined in detail. They contribute to increase the overall resistance of the filtered flow but the viscous contribution is seen smallest and is expected to be smaller in higher Reynolds numbers. These sub-filter contributions have been seen to depend on the filter scale and the local filtered magnitude of the velocity rather than the gradient of velocity. The presently documented results will be useful in developing and validating methods and modells for turbulent flows near boundary including those with small boundary irregularities that cannot be adequately be represented.

Acknowledgement

The initial part of the work was conducted when the first two authors were visiting fellows at the Center of Turbulence Research, Stanford University and the fourth author was a Japan Society of Promotion of Science (JSPS) post doctoral fellow at the Environmental Fluid Mechanics Laboratory of Stanford University. We are grateful to CTR and JSPS for financial support and to Prof. P. Moin, Prof. P. Bradshaw of Mechanical Engineering Department and Prof. R.L. Street of EFML for providing the opportunity and for various helpful discussion and useful suggestions.

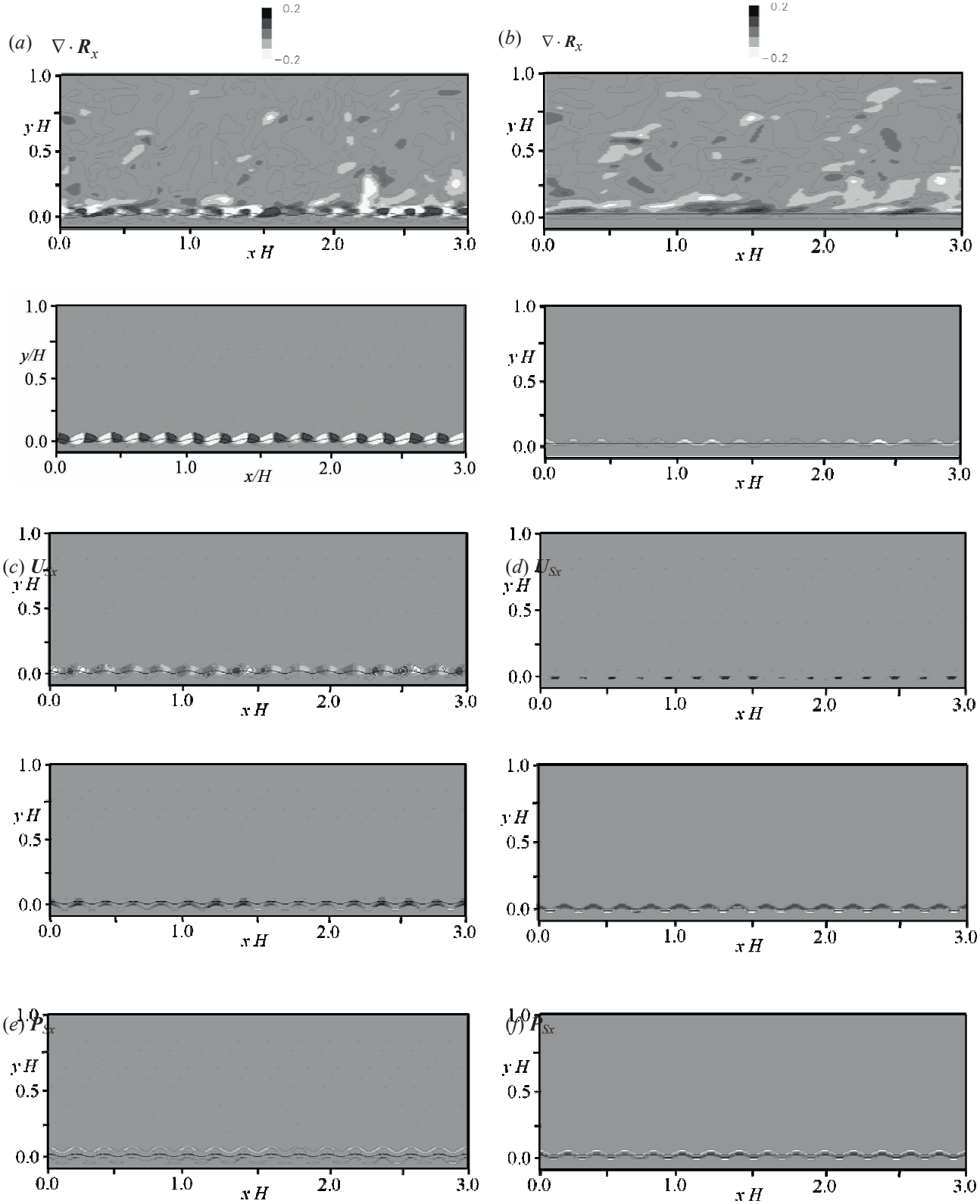

Fig. 28 Instantaneous distributions of sub-filter boundary terms in plane z=0.5B of FR3 compared with sub-filter stresses in plane z=0.5B. (*a*) $\nabla \cdot \boldsymbol{R}_x$ filter CF2, (*b*) $\nabla \cdot \boldsymbol{R}_x$ filter PF, (*c*) U_{sx} filter CF2, (*d*) U_{sx} filter PF, (*e*) P_{sx} filter CF2, (*f*) P_{sx} filter PF, (*g*) T_{sx} filter CF2, (*h*) T_{sx} filter PF, (*i*) $\nabla \cdot \tau_{Sx}$ filter CF2, (*j*) $\nabla \cdot \tau_{Sx}$ filter PF.

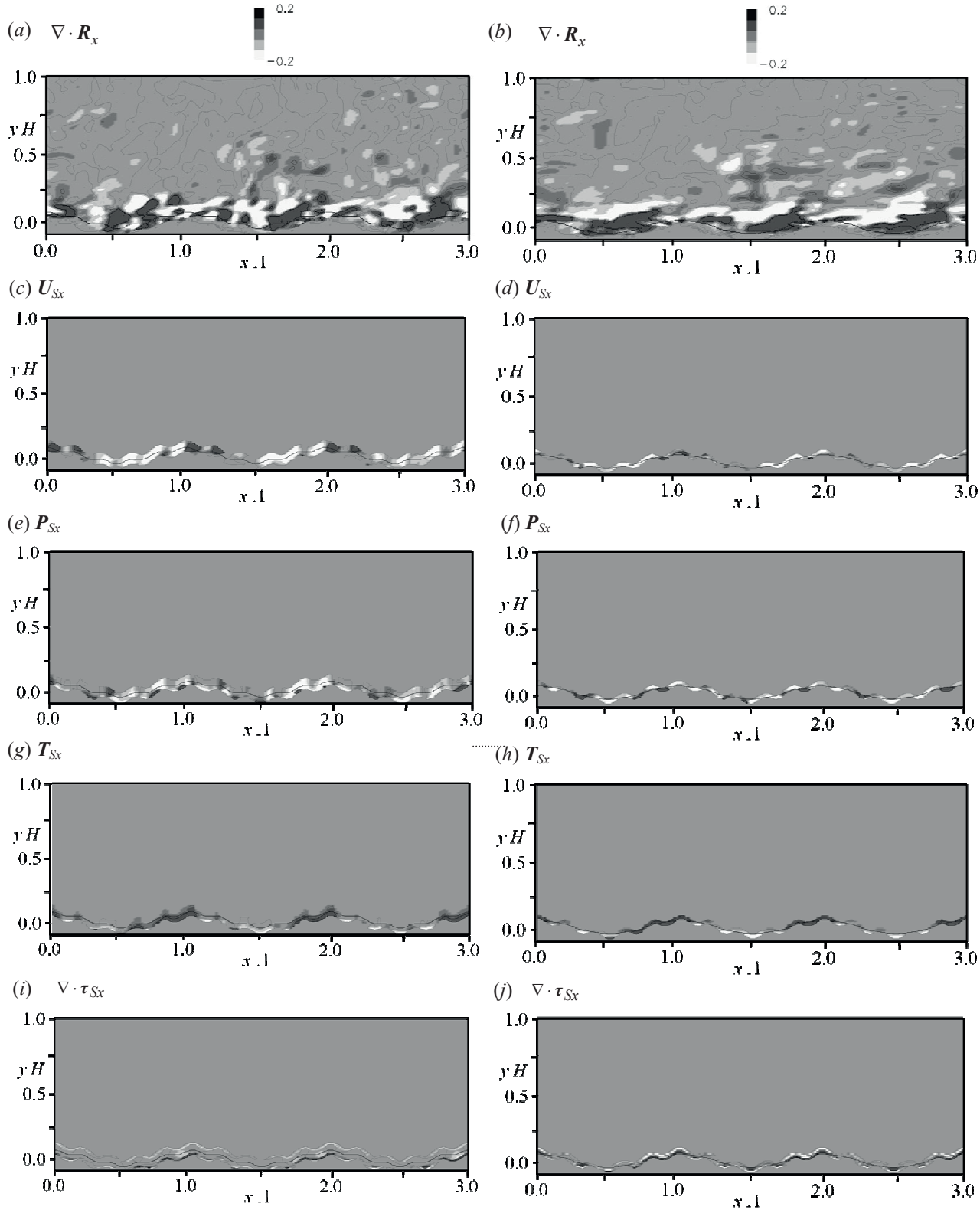

Fig. 32 Instantaneous distributions of sub-filter boundary terms in plane z=0.5B of WR3 compared with sub-filter stresses in plane z=0.5B. (*a*) $\nabla \cdot \boldsymbol{R}_x$ filter CF2, (*b*) $\nabla \cdot \boldsymbol{R}_x$ filter PF, (*c*) U_{sx} filter CF2, (*d*) U_{sx} filter PF, (*e*) P_{sx} filter CF2, (*f*) P_{sx} filter PF, (*g*) T_{sx} filter CF2, (*h*) T_{sx} filter PF, (*i*) $\nabla \cdot \tau_{Sx}$ filter CF2, (*j*) $\nabla \cdot \tau_{Sx}$ filter PF.

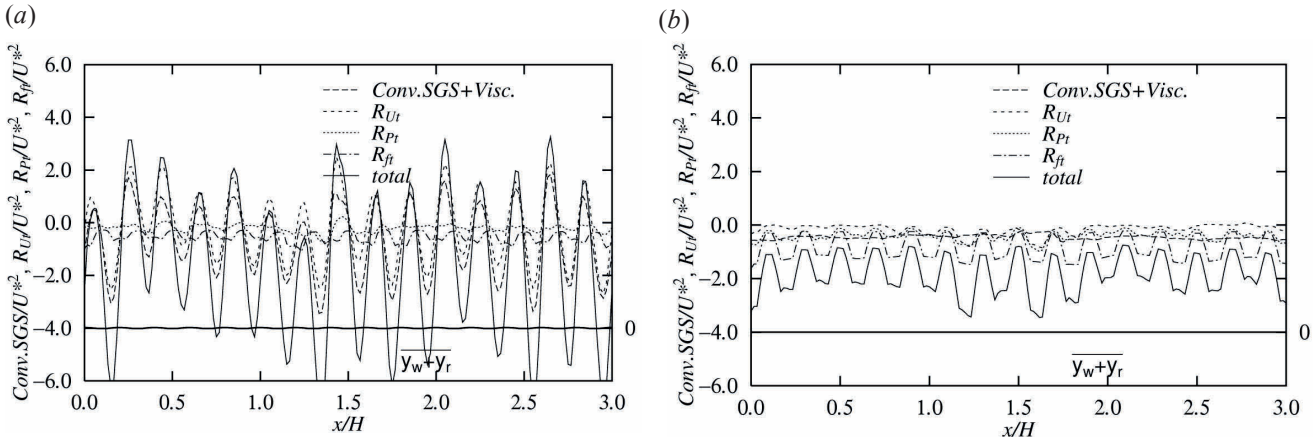

Fig. 33 Instantaneous resistance on the filtered boundarydue to sub-filter boundary terms compared with the conventional SGS terms and resolved viscous stress of FR3. (*a*) filter CF2 , (*b*) filter PF, , $\left(\boldsymbol{R}_{nt} + 2\nu\overline{S}_{nt}\right)/U^{*2}$; , $R_{Ut}/U^{*}2$; , $R_{Ut}/U^{*}2$; , $R_{Ut}/U^{*}2$; , total.

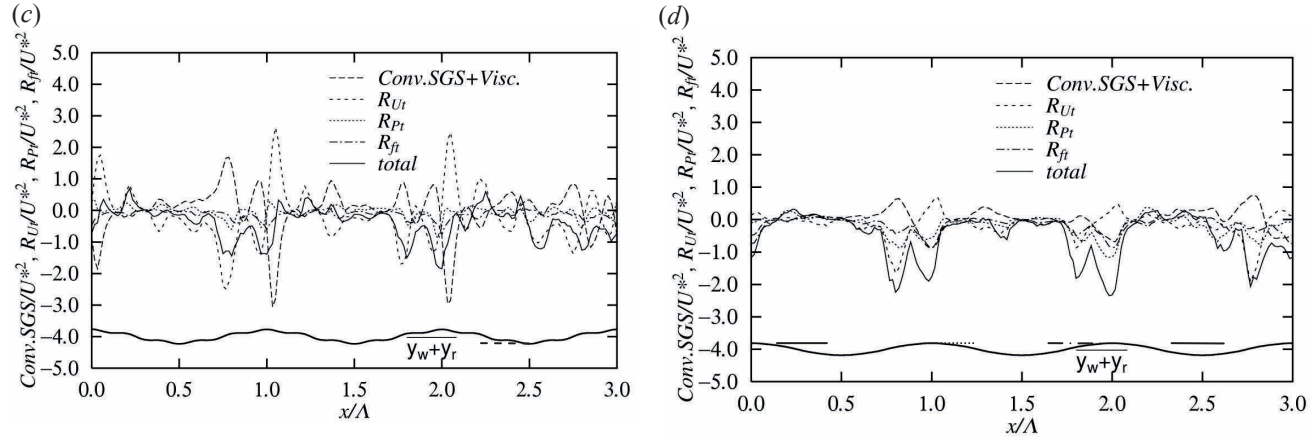

Fig. 34 Instantaneous resistance on the filtered boundarydue to sub-filter boundary terms compared with the conventional SGS terms and resolved viscous stress of WR3. (*a*) filter CF2 , (*b*) filter PF, legends are the same as Figure 33.

References

1) Townsend, A. A; "The Structure of Turbulent Shear Flow," 2nd ed., Cambridge Univ. Press, Cambridge, U.K. (1976)
2) Sagaut, P; "Large Eddy Simulation for Incompressible Flows." 3rd ed., Springer-Verlag, Berlin Heidelberg (2006)
3) Grinstein, F., Margolin, L. G. and Rider, W. J; "Implicit Large Eddy Simulation," Cambridge University Press, (2007)
4) Pope, S. B; "Turbulent Flows," Cambridge University Press, Cambridge, U.K. (2000)
5) Froehlich, J. and Rodi, W; "Introduction to large eddy simulation of turbulent flows," *Closure Strategied for Turbulent and Transitional Flows*, (ed. B.E. Launder & N.D. Sandham), 267-298 (2002)
6) Ghosal, S. and Moin, P; "The basic equations of the large-eddy simulation of turbulent flows in complex geometry," *J. Comput. Phys*, 118, 24-40 (1995)
7) Galdi, G. P. and Layton, W. J; " Approximating the larger eddies in fluid motion II: a model for space-filtered flow," *Math. Models and Meth. In Appl. Science*, 10,343-350 (2000)
8) Piomelli, U. and Balaras, E; "Wall-layer models for large-eddy simulations," *Annu. Rev. Fluid Mech*, 34, 349-374 (2002)
9) Buckles, J., Hanratty, T. J. and Adrian, R. J; "Turbulent flow over large-amplitude wavy surfaces," *J. Fluid Mech*. 140, 27-44 (1984)
10) Maass, C. and Schumann, U; "Numerical simulation of turbulent convection over wavy terrain," *Direct and Large-Eddy Simulation I*, ed. By P. R. Voke, L. Kleiser and J. P. Chollet. 287-297 Kluwer Academic (1994)
11) Hudson, J., Dykhno, L. and Hanratty, T; "Turbulent production in flow over a wavy wall," *Exp. Fluids*. 20, 257-265 (1996)
12) De Angelis, V., Lombardi, P. and Banerjee, S; "Direct numerical simulation of turbulent flow over a wavy wall," *Phys. Fluids,* 9(8), 2429-2441 (1997)
13) Cherukat, P., Na, Y., Hanratty, T.J. and Mclaughlin, J.B; "Direct numerical simulation of a fully developed turbulent flow over a wavy wall," *Theoret. Comput. Fluid Dynamics*, 11, 109-134 (1998)

14) Henn, D. S. & and Sykes, R. I; "Large-eddy simulation of flow over wavy surfaces," *J. Fluid Mech*, 383, 75-112 (1999)
15) Calhoun, R. J. and Street, R. L; "Turbulent flow over wavy surface: Neutral case," *J. Geophy. Res*, 106, 9277-9293 (2001)
16) Miyake, Y., Tsujimoto, K. and Nakaji, M; "Direct numerical simulation of rough-wall heat transfer in a turbulent channel flow," *Int J. Heat and Fluid Flow*, 22, 237-244 (2001)
17) Leonardi, S. Orlandi, P. Smalley, R. J. Dieidi, L. and Antonia, R. A; "Direct numerical simulatio of turbulent chael flow with trasverse square bars o one wall," *J. Fluid Mech* .491, 229-238 (2003)
18) Ashrafian, A , Andersson, H. I. & Manhart, M; "DNS of turbulent flow in a rod-roughened channel. " *International Journal of Heat and Fluid Flow*. 25, 373-383 (2004)
19) Nagano, Y., Hattori, H. & Houra, T; "DNS of velocity and thermal fields in turbulent channel flow with transverse-rib roughness," *Int J. Heat and Fluid Flow* 25, 393-403 (2004)
20) Choi, H. S. & Suzuki, K; "Large eddy simulation of turbulent flow and heat transfer in a channel with one wavy wall, " *J. Heat and Fluid Flow*. 26, 681-694 (2005)
21) Ikeda, T. & P. A. Durbin; "Direct simulations of a rough-wall channel flow," *J. Fluid Mech*. 571, 235-263 (2007)
22) Orlandi, P. & Leonardi, S; "Direct numerical simulation of three-dimensional turbulent rough channels:parameterization and flow physics, " *J.Fluid Mech*. 606, 399-415(2008)
23) Raudkivi, A. J; *Loose boundary hydraulics*, Balkema, Rotterdam, The Netherlands(1998)
24) Zedler, E.A. & Street, R. L; "Large-Eddy simulation of sediment transport: currents over ripples, " *J. Hydraul. Engrg.* 127, 444–452 (2001)
25) Schlichting, H; "Experimentelle Untersuchungen zum Rauhigkeitsproblem, " *Ing. Arch*. 7, 1-34 (1936)
26) Jimenez, J; "Turbulent flows over rough walls, " *Annu. Rev. Fluid Mech*. 36, 173-196(2004)
27) Tseng, Y. H. & Ferziger, J. H; "A ghost-cell immersed boundary method for flow in complex geometry, " *J. Comp. Phys*. 192(2), 593-623(2003)
28) Nakayama, A. & Yokojima, S; "Direct numerical simulation of the fully developed open-channel flow at subcritical Froude numbers, DNS/LES Progress and Challenges --- Third AFOSR International Conference, " *Arlington, Texas* , 569-576(2001)
29) Zhang, Y., Street, R. L. & Koseff, J. R; "A non-staggered grid, fractional step method for time-dependent incompressible Navier–Stokes equations in curvilinear coordinates, " *J. Comput. Phys.* 114, 18–33(1994)
30) Inagaki, M. & Abe, K; "An improvement of prediction accuracy of large eddy simulation on collocated grids, " *Transact. JSME B* . 64(623), 1981-1988 (in Japanese) (2004)
31) Kajishima, T; "Finite-difference method for convective terms using non-uniform grid, "*Trans. JSME B* 65, 1607–1612 (in Japanese) (1999)
32) Moser, R. D., Kim, J. & Mansour, N; "Direct numerical simulation of turbulent flows up to Ret=590, " *Phys. Fluids*. 11, 943-945(1999)
33) Nakayama, A. & Sakio, K; "Simulation of Flows Over Wavy Rough Boundaries, " *Center for Turbulence Research, Annual Research Briefs, Stanford University/NASA, Ames Research Center*. 313-324(2002)
34) Raupach, M. R., Antonia, R. A. & Rajagopalan, S; "Rough-wall turbulent boundary layers, " *Appl. Mech. Rev*. 44, 1-25(1991)
35) Schultz, M.P. & Flack, K.A; "Turbulent boundary layers on a systematically varied rough wall," *Phys. Fluids*, 21, 015104-1-9(2009)
36) Komori, S., Nagaosa, R., Murakami, Y., Chiba, S., Ishii, K. & Kuwahara, K; "Direct numerical simulation of three-dimensional open-channel flow with zero-shear gas-liquid interface," *Phys. Fluids A*, 5(1), 115-125(1993)
37) Schlichting, H; *Boundary-Layer Theory*, 7th ed. McGraw-Hill, New York (1979)
38) Colebrook, C.F; "Turbulent flow in pipes with particular reference to the transition region between the smooth and rough pipe laws," *J. Inst. Civ. Eng.* 11, 133-156(1939)
39) Gong, W., Taylor, P. A. & Doernbrack, A; "A turbulent boundary-layer flow over fixed aerodynamically rough two-dimensional sinusoidal waves," *J. Fluid Mech*. 312, 1-37(1996)
40) Agelinchaab, M. & Tachie, M.F; "PIV study of adverse and favorable pressure gradient turbulent flows over transverse ribs," *J. Fluids Engnrg*. 130(11), 11305-1-12(2008)
41) Vreman, A. W; "The adjoint filter operator in large-eddy simulation of turbulent flow," *Phys. Fluids*. 16(6), 2012-2022(2004)
42) Bhattacharya, A., Das, A. & Moser, R. D; "A filtered-wall formulation for large-eddy simulation of wall-bounded turbulence," *Phys. Fluids* 20(11), 115104-1-16(2008)
43) Natrajan, V.K. & Christensen, K.T; "The role of coherent structures in subgrid-scale energy transfer within the log layer of wall turbulence," *Phys. Fluids* 18(6), 065104-1-24(2006)
44) Nakagawa. & Hanratty; "Particle image velocimetry measurements of flow over a wavy wall," *Phys Fluids* . 13, 3504-3507(2001)
45) Whitaker, S; "Advances in theory of fluid motion in porous media," *Ind. Eng. Chem*. 61, 14-28(1969)
46) Gray, W. G. & Lee, P. C. Y; "On the theorems for local volume averaging of multiphase system," *Int. J. Multiphase Flow*. 3, 333-340(1977)
47) Nakayama, A., Hori, K. & Street, R.L; "Filtering and LES of flow over irregular rough boundary," Proc. Summer 2004 Program, Center for Turbulence Research, NASA/Stanford University, 145-156(2004)
48) Shen, L. & Yue, D. K. P; "Large-eddy simulation of free-surface turbulence," *J. Fluid Mech*. 440, 75-116(2001)
49) Hodges, B. R. & Street, R. L; "On simulation of turbulent nonlinear free-surface flows," *Journal of Computational Physics.*151, 425-457(1997)